



**HAL**  
open science

# The signature of inner-core nucleation on the geodynamo

Maylis Landeau, Julien Aubert, Peter Olson

► **To cite this version:**

Maylis Landeau, Julien Aubert, Peter Olson. The signature of inner-core nucleation on the geodynamo. *Earth and Planetary Science Letters*, 2017, 465, pp.193-204. 10.1016/j.epsl.2017.02.004 . insu-02918346

**HAL Id: insu-02918346**

**<https://insu.hal.science/insu-02918346>**

Submitted on 21 Aug 2020

**HAL** is a multi-disciplinary open access archive for the deposit and dissemination of scientific research documents, whether they are published or not. The documents may come from teaching and research institutions in France or abroad, or from public or private research centers.

L'archive ouverte pluridisciplinaire **HAL**, est destinée au dépôt et à la diffusion de documents scientifiques de niveau recherche, publiés ou non, émanant des établissements d'enseignement et de recherche français ou étrangers, des laboratoires publics ou privés.

# The signature of inner-core nucleation on the geodynamo

Maylis Landeau<sup>a,b,\*</sup>, Julien Aubert<sup>c</sup>, Peter Olson<sup>a</sup>

<sup>a</sup>*Department of Earth and Planetary Sciences, Johns Hopkins University, Olin Hall, 3400 N. Charles Street, Baltimore, MD 21218, USA*

<sup>b</sup>*Department of Applied Mathematics and Theoretical Physics, University of Cambridge, Cambridge CB3 0WA, United Kingdom.*

<sup>c</sup>*Institut de Physique du Globe de Paris, Sorbonne Paris Cité, Université Paris-Diderot, CNRS, 1 rue Jussieu, F-75005 Paris, France.*

---

## Abstract

Energy considerations indicate that the power delivered to the present-day geodynamo comes mainly from the growth of the solid inner core, through light element and latent heat releases. The nucleation of the inner core was, therefore, a major transition for the geodynamo. Here, we use numerical dynamo simulations linked by thermochemical evolution of the core to investigate the effects of inner-core nucleation (ICN) on the geodynamo, and identify possible ICN footprints in the palaeomagnetic field. Our results suggest that a strong-field dipole-dominated dynamo prior and after ICN (the uniformitarian scenario) is most likely. We predict little footprint of ICN on the surface field intensity, consistent with the observed lack of a long-term trend in paleointensity data. Instead, we find that the best proxy for inner-core growth is an increase in axial octupole strength with age, from present-day to ICN, which might be resolvable in the palaeomagnetic record. We confirm the existence of weak-field, multipolar dynamos prior to ICN, suggesting the dynamo might have transiently reached a weak-field state (the catastrophic scenario). The narrow stability domain of these weak-field dynamos implies that the catastrophic scenario is less probable than the uniformitarian scenario.

*Keywords:* geodynamo; weak-field vs strong-field dynamo; inner-core nucleation; geomagnetic field on long time scales; paleointensity; Geocentric Axial Dipole.

---

## 1. Introduction

The time at which Earth's inner core nucleated marked a major transition for core history, not only affecting the structure of the core but also inducing a sharp change in core energetics and in the powering of the geodynamo. Energy considerations indicate that the present-day geodynamo is mainly powered by inner-core solidification, through latent heat and light element releases at the inner-core boundary (ICB) (Lister, 2003; Labrosse, 2015). In contrast, before the nucleation of a solid inner core, the geodynamo was powered by secular cooling alone, possibly helped by magnesium precipitation (O'Rourke and Stevenson,

---

\*Corresponding author; email: landeau@damtp.cam.ac.uk  
Preprint submitted to Elsevier

December 25, 2016

2016; Badro et al., 2016) or tidal deformations (Le Bars et al., 2011). As a result, the power available for the dynamo was smaller prior to ICN than at present-day by a factor up to 100 (Stevenson et al., 1983; Labrosse, 2003).

Core thermal evolution models, which are based on energy and entropy balances in the core (e.g. Labrosse, 2003; Lister, 2003), provide constraints on the age of ICN. However, the resulting range of possible values is broad, especially with the ongoing controversies about the value of core thermal conductivity (de Koker et al., 2012; Pozzo et al., 2013; Gomi et al., 2013; Ohta et al., 2016; Konôpková et al., 2016). Recent studies, based on first-principle computations (Gomi et al., 2013; Ohta et al., 2016) or experiments (Gomi et al., 2013; Ohta et al., 2016), point towards a high value of the thermal conductivity two or three times higher than previous estimates; however, experiments by Konôpková et al. (2016) suggest a much lower thermal conductivity. Most recent core evolution models that use upward revision of the thermal conductivity predict a young inner core, with ICN age smaller than 1 – 1.5 Ga (Labrosse, 2015; Davies, 2015; Olson et al., 2015).

Meanwhile, advances in paleointensity measurements on single grain samples have revealed that the geodynamo was active 3.5 Ga (Tarduno et al., 2010; Biggin et al., 2011) or even 4.2 Ga ago (Tarduno et al., 2015), indicating that ICN likely occurred during a time covered by palaeomagnetic data.

The above developments pose multiple, still unresolved, questions about the history of the geodynamo. The question that has received the most attention is whether ICN induced changes in magnetic field properties, leaving footprints in the palaeomagnetic record, and providing independent constraints on ICN age. Another question, perhaps more fundamental than the first, is how to explain the enigmatic lack of controversial trend in the paleointensity record during the last two billion years (Smirnov et al., 2016).

In this paper, we use a series of numerical dynamo simulations linked by core energetics, in order to investigate the effects of ICN on the geodynamo and address the above questions. In the following, we assume that thermal convection was the only power source for the geodynamo during the several hundred million years that preceded ICN, a plausible scenario according to thermal evolution models (Driscoll and Bercovici, 2014; Olson et al., 2015).

## 2. State of the art on ICN palaeomagnetic signatures

It has long been proposed that the sharp change in power at ICN could have left a footprint in the paleointensity record, with a weaker field prior to ICN and a stronger field just after ICN (Stevenson et al., 1983; Hale, 1987). This expected drop in field intensity with age motivated hunts for ICN in the paleointensity record (e.g. Hale, 1987; Valet et al., 2014; Biggin et al., 2015). A few investigations have claimed to detect a decrease in field intensity with age, interpreted as a footprint of ICN, but its location varies from one study to the other: Biggin et al. (2015) locate the decrease between 1 Ga and 1.5 Ga, with a field minimum around 1.5

64 Ga, Macouin et al. (2004) argue for a decrease within 0.3–1 Ga, and Valet et al. (2014) find a field minimum  
65 around 1.8–2.3 Ga. Other palaeomagnetic investigations argue for the absence of clear long-term trend  
66 in the paleointensity record within the Precambrian period (Selkin and Tauxe, 2000; Tauxe, 2006; Smirnov  
67 et al., 2016). Furthermore, the average of the Precambrian dipole moment and its variability ( $49 \pm 31 \text{ ZAm}^2$   
68 according to the PINT database, Biggin et al., 2015) are indistinguishable, within uncertainties, with the  
69 0–300 Ma dipole moment of  $46 \pm 32 \text{ ZAm}^2$  determined by Selkin and Tauxe (2000), as well as the  $49 \text{ ZAm}^2$   
70 average dipole moment determined by Wang et al. (2015) for 0–5 Ma. In summary, the interpretation of  
71 the paleointensity record in relation to ICN is still an unsettled and ongoing debate.

72 Another possible signal probe of ICN is the surface field morphology. Although most palaeomagnetic  
73 investigations suggest that the surface field has been dominated by an axial dipole for the last two billion years  
74 (Evans, 2006; Veikkolainen and Pesonen, 2014; Biggin et al., 2015), anomalies in palaeomagnetic inclinations  
75 have been attributed to a stronger octupole during the Precambrian (Kent and Smethurst, 1998; Veikkolainen  
76 and Pesonen, 2014), a potential ICN footprint (Bloxham, 2000; Heimpel and Evans, 2013).

77 Because the interpretation of palaeomagnetic data remains controversial, modelling the evolution of the  
78 geodynamo is particularly useful to guide the search for ICN in the palaeomagnetic record. Numerical dynamo  
79 investigations have shown that the absence of an inner core may favor unusual field structures, superimposed  
80 to the axial dipole, including the axial quadrupole producing a field localized in one hemisphere (Landeau and  
81 Aubert, 2011; Hori et al., 2014) or the axial octupole (Heimpel and Evans, 2013). However, a full modelling  
82 of the evolution of the geodynamo field morphology is still missing, and is key to testing the Geocentric Axial  
83 Dipole (GAD) hypothesis on which continental drift reconstructions rely (Evans, 2013).

84 Theoretical predictions of the effect of ICN on paleointensity have been obtained by coupling core ener-  
85 getics with dynamo scalings (Olson, 1981; Stevenson et al., 1983; Aubert et al., 2009). Results from dynamo  
86 simulations have shown that the field intensity evolves as the available power to the power 1/3 (Christensen  
87 and Aubert, 2006; Christensen et al., 2009; Aubert et al., 2009). This scaling satisfactorily explains observa-  
88 tions of magnetic field strength in planets and stars (Christensen et al., 2009). Incorporating this power-based  
89 scaling into core evolution models, Aubert et al. (2009) have shown that the cooling of the core on geological  
90 time scales provides enough power to maintain a strong dipole field (i.e. of same order as the present-day  
91 field) prior to ICN and as late as  $\sim 3.5\text{Ga}$ , consistently with palaeomagnetic observations (Tarduno et al.,  
92 2010; Biggin et al., 2011). Aubert et al. (2009) predicted that the sharp change in available power due to ICN  
93 induced a sudden change in internal field intensity, with a field smaller by up to a factor of  $\sim 4$  prior to ICN  
94 compared to just after ICN. On the basis of an empirical scaling law relating the internal and surface field  
95 intensities, Aubert et al. (2009) found that the surface intensity weakens by a factor of 2 or less near ICN  
96 relative to present-day conditions. They attributed the smaller decrease in surface intensity to the shallowing

97 of the dynamo region with age, which partially compensates the overall loss of dynamo power.

98 In this study, we investigate the history of the geodynamo and the signature of ICN at the Earth's  
99 surface by combining the energetics of the core with dynamo simulations. Whereas Aubert et al. (2009)  
100 implement dynamo scalings into core evolution models, here, we directly apply core evolution models on  
101 dynamo simulations that model the present-day geodynamo. Because this new procedure does not rely on  
102 dynamo scalings, it can be used to investigate the evolution of any dynamo property with age, and pinpoint  
103 more precisely the effect of ICN on the morphology and intensity of the surface palaeomagnetic field. [We  
104 note that modelling the long-term evolution of the reversal frequency is out of the scope of the present study.](#)  
105 A similar general recipe was used recently by Driscoll (2016) whose results are compared to ours in Section  
106 6.

### 107 3. Procedure

#### 108 3.1. General recipe

109 Our procedure consists of the following steps:

- 110 1. First, we compute two core evolution models. We integrate, backward in time, the formulation by  
111 Labrosse (2003) for core thermal evolution, subject to two CMB heat flux histories, to determine the  
112 evolution, with age, of key properties that affect the geodynamo: the inner-core radius, the power  
113 available for the dynamo, and the distribution of mass anomaly fluxes (Fig. 1).
- 114 2. Second, we select numerical simulations of the present-day geodynamo, based on "Earth-like" criteria  
115 defined in Christensen et al. (2010), in order that the magnetic fields of the present-day dynamo models  
116 conform to the morphology of the present-day geomagnetic field.
- 117 3. Third, we compute ancient dynamo simulations at a sequence of epochs, including post-ICN and pre-  
118 ICN ages. For this, we use the age-dependent properties from our core histories (step 1, Fig. 1), to  
119 compute the evolution of dimensionless geodynamo control parameters. We then apply ratios of past to  
120 present-day values of these dimensionless parameters (Fig. 3) to the present-day dynamo simulations  
121 isolated in step 2.
- 122 4. Fourth, we analyze the changes in magnetic field with age, relative to the present-day model, using  
123 output quantities defined in Section 3.6. For internal consistency, results are shown in terms of past-  
124 to-present dimensional quantity ratios.

#### 125 3.2. Core evolution model

126 Given the large uncertainties in the outer core thermal conductivity and the CMB heat flux, it is not  
 127 possible to uniquely determine the evolution of Earth’s core. Instead, we define two end-member core  
 128 evolution scenarios in order to test the sensitivity of our results to the core evolution model.

129 Several recent experimental and theoretical studies on core transport properties predict a rather high  
 130 thermal conductivity, with an average value in the range of 100 W/m/K (de Koker et al., 2012; Pozzo et al.,  
 131 2013; Gomi et al., 2013). The resulting heat flow along the adiabat is  $\sim 11 - 15$  TW, values that fall within  
 132 the range of possible CMB heat flow values (Lay et al., 2008). This allows for two possible states of the  
 133 present-day Earth’s core: either superadiabatic or subadiabatic at the CMB.

134 Our core first history, hereafter referred as History 1, assumes a superadiabatic and spatially uniform  
 135 CMB heat flux that is constant in time (i.e., constant with age). We choose  $Q = 13.1$  TW for the total  
 136 CMB heat flow, equivalent to a global mean heat flux of  $q=86$  mW/m<sup>2</sup>. This value is the time average  
 137 CMB heat flux produced by the three mantle GCMs with plate motion constraints described in Olson et al.  
 138 (2015), all of which generate large-scale patterns of mantle heterogeneity above the CMB that are similar  
 139 to the seismically observed large low shear velocity provinces. As shown below, the core evolution model of  
 140 Labrosse (2003) predicts an ICN age near 700 Ma and yields superadiabatic thermal conditions for the last  
 141 1500 Ma with this CMB heat flux, assuming a core thermal conductivity of 100 W/m/K.

142 However, lower values for the CMB heat flow are possible (Lay et al., 2008) and would result in stabilizing  
 143 subadiabatic conditions at the CMB, in which case the constant CMB heat flux assumption of History 1  
 144 would preclude a convective dynamo prior to ICN. In order to model the effects of lower CMB heat flow  
 145 while allowing for a convective dynamo at all times, we have constructed a second CMB heat flow history,  
 146 referred to as History 2, in which the core is nearly adiabatic today and superadiabatic at pre-ICN times.  
 147 For History 2, we assume  $Q = 12 + 0.003\tau$  TW, where  $\tau$  is age before present-day in Ma. History 2 yields  
 148 approximately the same 700 Ma inner core age.

149 We have applied the core evolution model formulation by Labrosse (2003) to compute the history of the  
 150 core for both CMB heat flux histories, starting at the present-day and going back to 1500 Ma. As detailed  
 151 in Supplementary Material, integrating backward in time yields the evolution of the inner core radius  $r_i$ , the  
 152 ICB mass anomaly flux  $F_i$ , the CMB mass anomaly flux  $F_o$  and the power generated by buoyancy forces (i.e.  
 153 the power available for the dynamo)

$$\Phi = - \int_{V_s} \rho \mathbf{u} \cdot \mathbf{g} dV, \quad (1)$$

154 where  $V_s$  is the outer core volume,  $\mathbf{u}$  the velocity field and  $\mathbf{g}$  the gravitational field. .

155 Fig. 1 summarizes the important results for core Histories 1 and 2.

156 Multiple studies on paleo-length of day (l.o.d.) agree on a decrease of about 20 s/Ma in l.o.d. during  
 157 the last few hundreds million years, and a smaller, more uncertain, decrease during the Proterozoic (e.g.

158 Williams, 2000; Denis et al., 2011). In our core histories, we consider a uniform increase in  $\Omega$  with age  
 159 between 0 – 250 Ma, amounting to a change in l.o.d. of 20 s/Ma, and a constant rotation rate for ages larger  
 160 than 250 Ma.

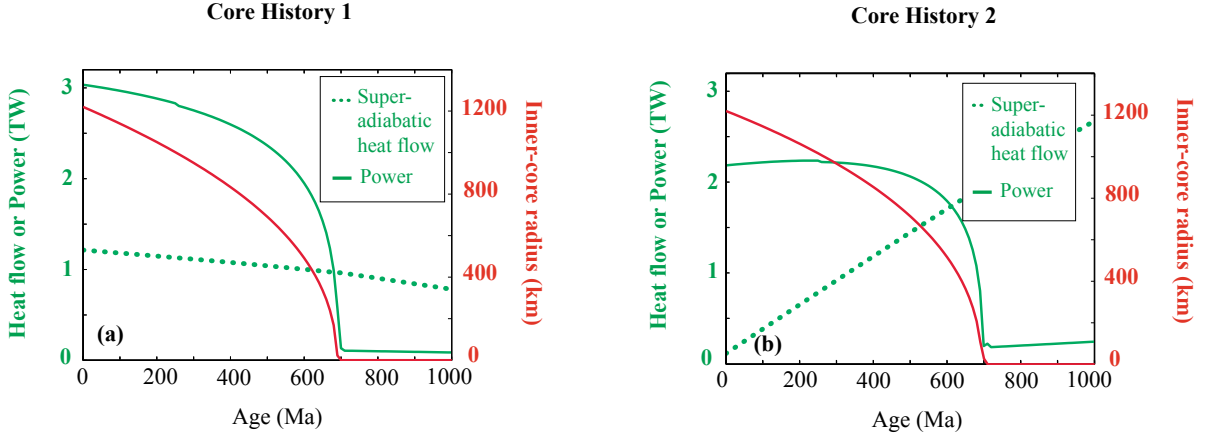


Figure 1: Thermal evolution models of the core with constant CMB heat flux (History 1, left) and CMB heat flux increasing with age (History 2, right) showing the evolution of the superadiabatic CMB heat flow  $Q - Q_a$  (dotted green curve), power generated by the buoyancy force and available for the dynamo  $\Phi$  (solid green curve) and inner-core radius  $r_i$  (red curve), all as functions of age.

### 161 3.3. Dynamo model and parameters

162 To model thermochemical convection and dynamo action in the outer core, we follow the approach in  
 163 Aubert et al. (2009). We use the numerical code PARODY-JA (Dormy et al., 1998; Aubert et al., 2008)  
 164 to solve numerically the mass, momentum and energy conservation equations, together with the induction  
 165 equation, for a Boussinesq, electrically conducting fluid in a self-gravitating, rotating shell between radii  $r_i$   
 166 and  $r_o$  (representing the inner-core and core-mantle boundaries, respectively). These equations govern the  
 167 evolution of the velocity field  $\mathbf{u}$ , the magnetic field  $\mathbf{B}$  and the codensity (or density anomaly) field  $C$  that  
 168 accounts for thermal and compositional density anomalies (Braginsky and Roberts, 1995) such that

$$C = \alpha\rho T + \beta\rho\xi, \quad (2)$$

169 where the temperature  $T$  and the light element mass fraction  $\xi$  are deviations from the mean adiabatic  
 170 temperature and the mean mass fraction in the outer core,  $\alpha$  and  $\beta$  are the thermal and compositional  
 171 expansion coefficients, and  $\rho$  is the outer core density. The temperature and mass fraction fields are assumed  
 172 to have the same effective diffusivity,  $\kappa$ . We impose a uniform density anomaly flux at the inner and outer

173 boundaries. This amounts to imposing a mass anomaly flux

$$F_i = - \int_{S_i} \kappa \frac{\partial C}{\partial r} dS \quad (3)$$

174 at the inner boundary, modeling the effect of latent heat and light element release at the ICB, and a mass  
175 anomaly flux

$$F_o = - \int_{S_o} \kappa \frac{\partial C}{\partial r} dS, \quad (4)$$

176 at the outer boundary, representing the effect of the superadiabatic heat flux imposed by the mantle on the  
177 core. The other boundary conditions are: no-slip for the velocity and electrically insulating for the magnetic  
178 field at the inner and outer boundaries.

179 To model the geodynamo prior to ICN, we use full-sphere dynamo simulations where the inner-core has  
180 been completely removed. In this specific case, we impose boundary conditions at the center that force  
181 the solution and its derivatives to be regular, as detailed in Landeau (2013); this solves the problem of the  
182 singularity at the center in spherical coordinates. This full-sphere implementation in the code PARODY-JA  
183 has been validated against theoretical solutions (Landeau, 2013) and against numerical benchmarks (Marti  
184 et al., 2014).

185 The mean density of Earth’s core evolved over geological time scales due to slow cooling of the core  
186 and light element enrichment as the inner core grows and contributes to driving core convection. Because  
187 these evolutionary effects operate on time scales much larger than the time scale relevant for core convection,  
188 they can be modeled numerically by internal buoyancy sources in a statistically stationary system (e.g.  
189 Braginsky and Roberts, 1995). Accordingly, we assume a constant and spatially uniform distribution of  
190 internal buoyancy sources, determined such that mass is conserved inside the shell (Aubert et al., 2009).

191 The system is then governed by six dimensionless control parameters: the ratio of inner to outer core  
192 radius, or aspect ratio,

$$\epsilon = \frac{r_i}{r_o}, \quad (5)$$

193 the ratio of inner-boundary mass anomaly flux to total mass anomaly flux, or buoyancy source distribution,

$$f_i = \frac{F_i}{F_i + F_o}, \quad (6)$$

194 the Prandtl and magnetic Prandtl numbers

$$Pr = \frac{\nu}{\kappa}, \quad Pm = \frac{\nu}{\eta}, \quad (7)$$

195 where  $\kappa$  and  $\eta$  are diffusivities for the codensity and magnetic field, respectively, the Ekman number, which  
196 measures the ratio of viscous to rotational effects, and the modified Rayleigh number, which measures the

197 vigor of convection,

$$E = \frac{\nu}{\Omega D^2}, \quad Ra_Q = \frac{g_o F}{4\pi\rho\Omega^3 D^4}, \quad (8)$$

198 where  $g_o$  is gravity at the outer boundary at  $r_o$ ,  $F = F_i + F_o$  is the total mass anomaly flux,  $\Omega$  the rotation  
199 rate,  $D$  the shell gap between the inner and outer boundaries, and  $\nu$  the viscosity of the outer core.

200 The Rayleigh number  $Ra_Q$  is a measure of the vigor of convection: for sufficiently supercritical convec-  
201 tion, it is proportional to the dimensionless power density  $p$  generated by the buoyancy forces, from which  
202 convection originates, such that (see Supplementary Material)

$$p = \gamma Ra_Q, \quad (9)$$

203 with

$$p = \frac{\Phi/V_s}{\rho\Omega^3 D^2}, \quad (10)$$

204 where  $\Phi$  is the power generated by buoyancy forces defined by (1),  $V_s$  the shell volume, and  $\gamma$  a constant  
205 that depends on the shell geometry and the boundary conditions (Supplementary Material). Note that, by  
206 definition, the convective power  $p$  measures the power available for convection and dynamo action, for which  
207  $Ra_Q$  is only an approximate proxy that does not account for variable shell geometry or variable buoyancy  
208 source distribution. The canonical Rayleigh number  $Ra = g_o \Delta C D^3 / \rho \nu \kappa$ , where  $\Delta C \equiv F / 4\pi \kappa D$ , is given  
209 by  $Ra = Ra_Q E^{-3} Pr^2$ . Unlike  $Ra$ ,  $Ra_Q$  has the advantage of being independent of the thermal and viscous  
210 diffusivities, and is therefore the relevant parameter to study convection in the limit of low Ekman and highly  
211 supercritical conditions (Christensen and Aubert, 2006).

212 As shown in Section 3.2, thermochemical evolution of the core implies that the rotation rate, the inner-  
213 core size, the buoyancy source distribution, and the dissipation vary over geological time scales. Therefore,  
214 four dynamo control parameters are functions of time (or age):  $\epsilon$ ,  $f_i$ ,  $Ra_Q$  and  $E$ .

### 215 3.4. Present-day dynamo simulations

216 To model the present-day geodynamo, we use two sets of simulation parameters (given in Table 1, Age 0  
217 Ma), one for each core history. In both simulations, the aspect ratio  $\epsilon$  is chosen equal to 0.35, its value in the  
218 present-day core. For the buoyancy source distribution  $f_i$ , we impose values equal to these predicted by our  
219 core Histories 1 and 2 to within 1%. The Ekman number is equal to  $3 \times 10^{-5}$  in both simulations, a value  
220 reasonably low compared to other published dynamo models (e.g. Driscoll, 2016; Hori et al., 2014; Heimpel  
221 and Evans, 2013) but sufficiently high to permit simulations at different ages with the two core histories.

222 We adjust the other parameters ( $Pr$ ,  $Pm$ ,  $Ra_Q$ ) so that our dynamo simulations produce a CMB field  
223 that resembles that of the present-day core field. For this, we use criteria formulated by Christensen et al.

224 (2010) to quantify the degree of resemblance of a dynamo model magnetic field with the geomagnetic field  
 225 at the CMB.

226 Christensen et al. (2010) measure the compliance of dynamo models to the historical geomagnetic field  
 227 in terms of four properties of the field up to spherical harmonic degree and order eight: the ratio of the  
 228 power in the axial dipole component to that in the rest of the field, the ratio between equatorially symmetric  
 229 and antisymmetric components, the ratio between zonal and non-zonal non-dipole components, and the  
 230 spatial concentration of magnetic flux, all at the CMB. These properties are factored into the definition of  
 231 a compliance parameter  $\chi^2$ , which varies typically between 0.3 and 20 in numerical dynamos. Excellent  
 232 compliance as defined by Christensen et al. (2010) corresponds to  $\chi^2 \leq 2$ . We choose present-day dynamo  
 233 parameters such that the compliance parameter  $\chi^2$  is equal to 1.4 and 0.7 (Table 1).

234 Fig. 2 illustrates morphological similarities between the geomagnetic field (Fig.2a) and the field produced  
 235 by our present-day dynamo simulations (Fig.2b,c). In both cases, the radial field is dominated by an axial  
 236 dipole, although significant deviations from axial and dipolar symmetries are present. For example, in the  
 237 geomagnetic field and the dynamo simulations, we see strong non-axial structures that form pairs of radial  
 238 field patches, antisymmetric with respect to the equator; these are the signature of columnar flows in the  
 239 shell. Other non-axial field structures form single patches, such as the reversed flux patches seen in the  
 240 Southern hemisphere in Fig.2a,b.

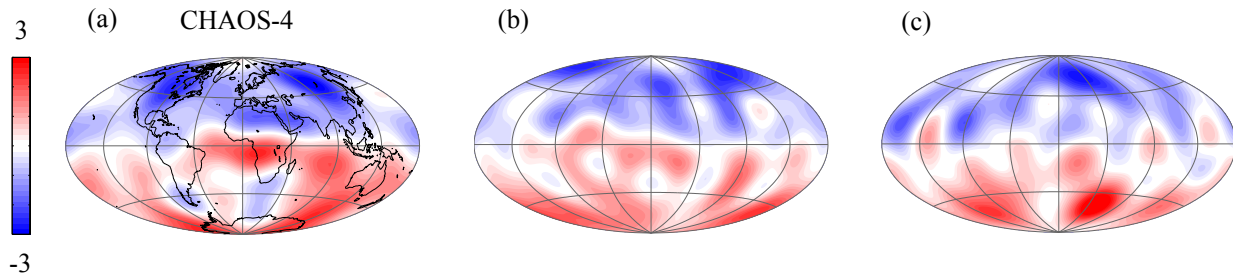


Figure 2: Radial magnetic field at the CMB up to degree eight, normalized by its root mean square value. (a) CHAOS-4 geomagnetic field model in 2010 (Olsen et al., 2014). (b,c) Snapshots from present-day dynamo simulations for History 1 and History 2, respectively (dynamo parameters given in Table 2 at age 0 Ma).

### 241 3.5. Ancient dynamo simulations

242 Starting from the above present-day dynamo simulations, we use our core evolution models (core Histories  
 243 1 and 2) to define a set of dynamo simulation parameters that model the geodynamo at earlier times, as  
 244 illustrated in Fig.3 and described in what follows.

245 First, from the core histories shown in Fig.1, we compute the evolution with age of the convective power  
 246  $p$  (equation (10)), the Ekman number  $E$  (equation (8)), the aspect ratio  $\epsilon$  (equation (5)) and the buoyancy

History	Age(Ma)	$\epsilon$	$f_i$	$E$	$Ra_Q$	$p$	$\chi^2$	$f_{\text{dip}}$	$\Lambda$	$ME/KE$	Regime	
1	0	0.350	0.93	$3 \times 10^{-5}$	$2.70 \times 10^{-5}$	$8.37 \times 10^{-6}$	1.4	0.44	19.92	2.55	SF	St
1	330	0.263	0.92	$2.2 \times 10^{-5}$	$1.16 \times 10^{-5}$	$4.85 \times 10^{-6}$	1.5	0.52	21.31	3.42	SF	St
1	540	0.178	0.90	$1.8 \times 10^{-5}$	$5.67 \times 10^{-6}$	$3.02 \times 10^{-6}$	2.7	0.57	24.21	4.99	SF	St
1	700	0.00	0.00	$1.2 \times 10^{-5}$	$4.32 \times 10^{-7}$	$1.39 \times 10^{-7}$	7.9	0.58	11.46	42.04	SF	St
		0.00	0.00	$1.2 \times 10^{-5}$	$4.32 \times 10^{-7}$	$1.39 \times 10^{-7}$	7.9	0.58	0.42	0.65	WF	St
1	1000	0.00	0.00	$1.2 \times 10^{-5}$	$3.31 \times 10^{-7}$	$9.31 \times 10^{-8}$	10.9	0.62	9.68	50.44	SF	St
		0.00	0.00	$1.2 \times 10^{-5}$	$3.31 \times 10^{-7}$	$9.31 \times 10^{-8}$	10.9	0.62	0.33	0.74	WF	Mt
2	0	0.350	0.99	$3 \times 10^{-5}$	$2.70 \times 10^{-5}$	$8.63 \times 10^{-6}$	0.7	0.41	17.31	2.02	SF	St
2	330	0.263	0.93	$2.2 \times 10^{-5}$	$1.38 \times 10^{-5}$	$5.84 \times 10^{-6}$	1.0	0.49	21.07	2.75	SF	St
2	540	0.178	0.87	$1.74 \times 10^{-5}$	$7.02 \times 10^{-6}$	$3.72 \times 10^{-6}$	2.5	0.53	26.37	4.33	SF	St
2	700	0.00	0.00	$1.2 \times 10^{-5}$	$7.20 \times 10^{-7}$	$2.77 \times 10^{-7}$	3.8	0.51	15.38	30.50	SF	St
		0.00	0.00	$1.2 \times 10^{-5}$	$7.20 \times 10^{-7}$	$2.77 \times 10^{-7}$	3.8	0.51	0.51	0.43	WF	Mt
2	1000	0.00	0.00	$1.2 \times 10^{-5}$	$9.22 \times 10^{-7}$	$3.80 \times 10^{-7}$	2.1	0.50	15.21	21.69	SF	St
		0.00	0.00	$1.2 \times 10^{-5}$	$9.22 \times 10^{-7}$	$3.80 \times 10^{-7}$	2.1	0.50	0.71	0.45	WF	Mt

Table 1: Parameters and diagnostics for dynamo simulations, [each simulation spanning between 1 and 2 magnetic diffusion times](#). See Section 3 for definition of the buoyancy source distribution  $f_i$ , the Ekman number  $E$ , the Rayleigh number  $Ra_Q$ , the convective power  $p$ , the relative dipole field strength  $f_{\text{dip}}$ , [the Elsasser number  \$\Lambda\$  and the mean ratio of magnetic to kinetic energies  \$ME/KE\$](#) . Two dynamo solutions are found at 700 Ma and 1000 Ma; the last two columns characterize the regime and the stability of the dynamo solutions: ‘SF’, ‘WF’, ‘St’ and ‘Mt’ for strong-field regime, weak-field regime, stable and metastable, respectively (see section 4.1 for definitions). We follow the definition of Christensen et al. (2010) for the compliance parameter  $\chi^2$ . In all simulations, we impose  $Pr = 1$  and  $Pm = 2.5$ .

247 source distribution  $f_i$  (equation (6)) relative to their present-day values (the subscript 0 denotes present-day  
 248 values). The resulting past-to-present day ratios characterizing the evolution of the geodynamo are shown in  
 249 Fig.3 and their values are given in Table 2 and Table 3.

250 We then select four age values (vertical dashed lines in Fig.3) such that two ancient dynamos have an  
 251 inner core (330 Ma, 540 Ma), one ancient dynamo is located right at ICN (700 Ma) and another one is located  
 252 well before the inner-core starts to nucleate (1000 Ma).

253 For each core history and each of these four ages, we define an ancient dynamo simulation such that  $E$ ,  $f_i$   
 254 and  $\epsilon$  are equal to their values in the present-day simulation times the past-to-present day ratios  $f_i/f_{i0}$ ,  $\epsilon/\epsilon_i$   
 255 and  $E/E_0$  predicted by the core history (Table 2 and Table 3) to within 2% error. We then adjust the value of  
 256 the Rayleigh number  $Ra_Q$  so that the ratio of past-to-present convective power in our dynamo series matches  
 257 the ratio  $p/p_0$  predicted by the core history (Table 2 and Table 3) to within 10% error. Note that relation (9)  
 258 implies that matching  $p/p_0$  or  $Ra_Q/Ra_{Q_0}$  is equivalent for sufficiently supercritical conditions (satisfied only  
 259 for our post-ICN simulations). The resulting control parameter values for these ancient dynamo simulations  
 260 are given in Table 1.

261 Several reasons motivate the use of the convective power  $p$  to scale our dynamo models to the Earth,  
 262 instead of  $Ra_Q$ . First, numerical (e.g. Christensen and Aubert, 2006; Olson and Christensen, 2006; Aubert  
 263 et al., 2009; Davidson, 2013) and natural dynamos (Christensen et al., 2009) provide evidence that the  
 264 convective power controls the self-sustained field intensity, which is determined through a balance between  
 265 the convective power and the Ohmic dissipation. Second, practical reasons add to the above physical reason:  
 266 scaling the dynamo model using past-to-present day ratios of  $Ra_Q$  would produce pre-ICN simulations located  
 267 below the onset of dynamo action or even the onset of convection. Using ratios of the deviation from the  
 268 onset of convection is possible, but requires knowing precisely the critical Rayleigh number for convection  
 269 onset, which would add another step in the recipe.

### 270 3.6. Output parameters

271 For each present-day and ancient dynamo simulation, we compute several outputs that characterize the  
 272 structure and intensity of the magnetic field. The mean internal field intensity  $B_{\text{rms}}$  is measured as the  
 273 time-averaged root-mean square (rms) field in the shell, such that

$$B_{\text{rms}} = \left( \frac{1}{V_s} \left\langle \int_{V_s} \mathbf{B}^2 dV \right\rangle \right)^{1/2}, \quad (11)$$

274 where  $\mathbf{B}$  is the dimensional magnetic field,  $V_s$  the shell volume and the angled brackets indicate a time-  
 275 averaging operator.

Age (Ma)	$\epsilon/\epsilon_0$	$f_i/f_{i_0}$	$E/E_0$	$p/p_0$	IC
<b>0</b>	1.000	1.00	1.00	1.00	Y
200	0.861	1.00	0.83	0.71	Y
<b>330</b>	0.752	0.99	0.73	0.57	Y
400	0.683	0.99	0.69	0.51	Y
<b>540</b>	0.509	0.98	0.59	0.37	Y
600	0.403	0.96	0.54	0.30	Y
<b>700</b>	0.000	0.00	0.39	$1.5 \times 10^{-2}$	N
800	0.000	0.00	0.39	$1.1 \times 10^{-2}$	N
<b>1000</b>	0.000	0.00	0.39	$9.8 \times 10^{-3}$	N
1200	0.000	0.00	0.39	$8.3 \times 10^{-3}$	N
1400	0.000	0.00	0.39	$6.8 \times 10^{-3}$	N

Table 2: Evolution of dynamo parameters as predicted by core History 1 (see Section 3 for details). The subscript 0 denotes present-day parameter values. The present-day values of  $f_i$ ,  $\epsilon$ ,  $E$  and  $p$  are equal to 0.94, 0.35,  $2.71 \times 10^{-15}$  and  $8.32 \times 10^{-13}$ , respectively, in core History 1. Bold characters indicate age values at which we compute dynamo simulations. The last column indicates the presence of an inner core: 'Y' for ages with an active inner core and 'N' for ages without an active inner core.

Age (Ma)	$\epsilon/\epsilon_0$	$f_i/f_{i_0}$	$E/E_0$	$p/p_0$	IC
<b>0</b>	1.000	1.00	1.00	1.00	Y
200	0.870	0.97	0.84	0.77	Y
<b>330</b>	0.766	0.95	0.74	0.66	Y
400	0.700	0.94	0.70	0.60	Y
<b>540</b>	0.528	0.90	0.60	0.47	Y
600	0.423	0.88	0.55	0.39	Y
<b>700</b>	0.022	0.00	0.42	$3.1 \times 10^{-2}$	N
800	0.000	0.00	0.39	$3.1 \times 10^{-2}$	N
<b>1000</b>	0.000	0.00	0.39	$3.8 \times 10^{-2}$	N
1200	0.000	0.00	0.39	$4.4 \times 10^{-2}$	N
1400	0.000	0.00	0.39	$5.1 \times 10^{-2}$	N

Table 3: Same as for Fig.2 but for core History 2. The present-day values of  $f_i$ ,  $\epsilon$ ,  $E$  and  $p$  are equal to 0.99, 0.35,  $2.71 \times 10^{-15}$  and  $7.29 \times 10^{-13}$ , respectively, in core History 2.

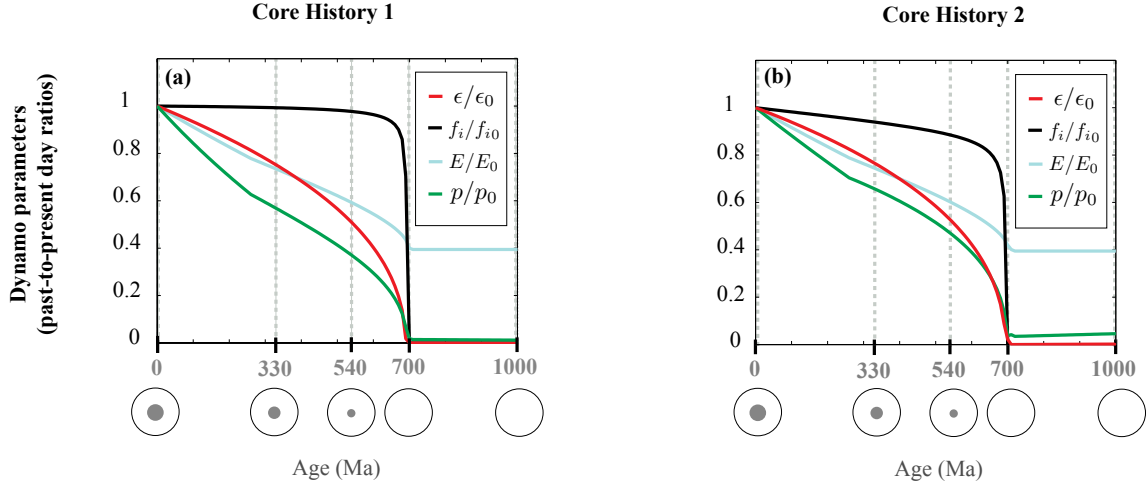


Figure 3: Evolution of geodynamo parameters (aspect ratio  $\epsilon$ , Ekman number  $E$ , convective power  $p$  and buoyancy source distribution  $f_i$ ) relative to their present-day values (denoted by the subscript 0), as deduced from core History 1 (left) and core History 2 (right). Grey vertical dashed lines locate ages where dynamo simulations are computed; schematic grey icons show the corresponding core structure, filled black circles representing the inner core.

276 The surface field intensity is measured through the time-averaged dipole moment  $M$  defined as follows:

$$M = \frac{4\pi r_o^3}{\sqrt{2}\mu} B_{\text{dip}}, \quad (12)$$

277 where  $\mu$  is the magnetic permeability, and  $B_{\text{dip}}$  the time-averaged rms dipole field intensity at  $r_o$ .

278 The relative dipole field strength  $f_{\text{dip}}$  is measured as the time-average ratio of the rms dipole field in-  
 279 tensity to the rms of the total field on the outer shell boundary. We also compute time-averaged ratios of  
 280 Schmidt-normalized Gauss coefficients: the ratio  $G_2$  of axial quadrupole to axial dipole and the ratio  $G_3$   
 281 of axial octupole to axial dipole. We compute the Elsasser number  $\Lambda = B_{\text{rms}}^2 / \rho\mu\eta\Omega$ , which measures the  
 282 relative strength of the Lorentz and Coriolis forces, and the time-averaged ratio of magnetic to kinetic energy  
 283  $ME/KE$ .

284 The quantities  $f_{\text{dip}}$ ,  $ME/KE$ ,  $G_2$  and  $G_3$  are dimensionless ratios of output quantities; therefore, no  
 285 scaling is needed to extrapolate the results from dynamo simulations to the geodynamo. This is not true for  
 286 the field intensities or the dipole moment whose extrapolation to the Earth implies the choice of a scaling  
 287 procedure. To avoid any arbitrary nondimensionalization of the magnetic field, we show the results in terms  
 288 of ratios of past-to-present day dimensional values. With this choice, the results are independent of the  
 289 characteristic time scale and length scale chosen to define the control dynamo parameters (5)-(8).

290 4. Evolution dynamo regime and magnetic field morphology with age

291 4.1. Geodynamo regimes: strong-field versus weak-field states

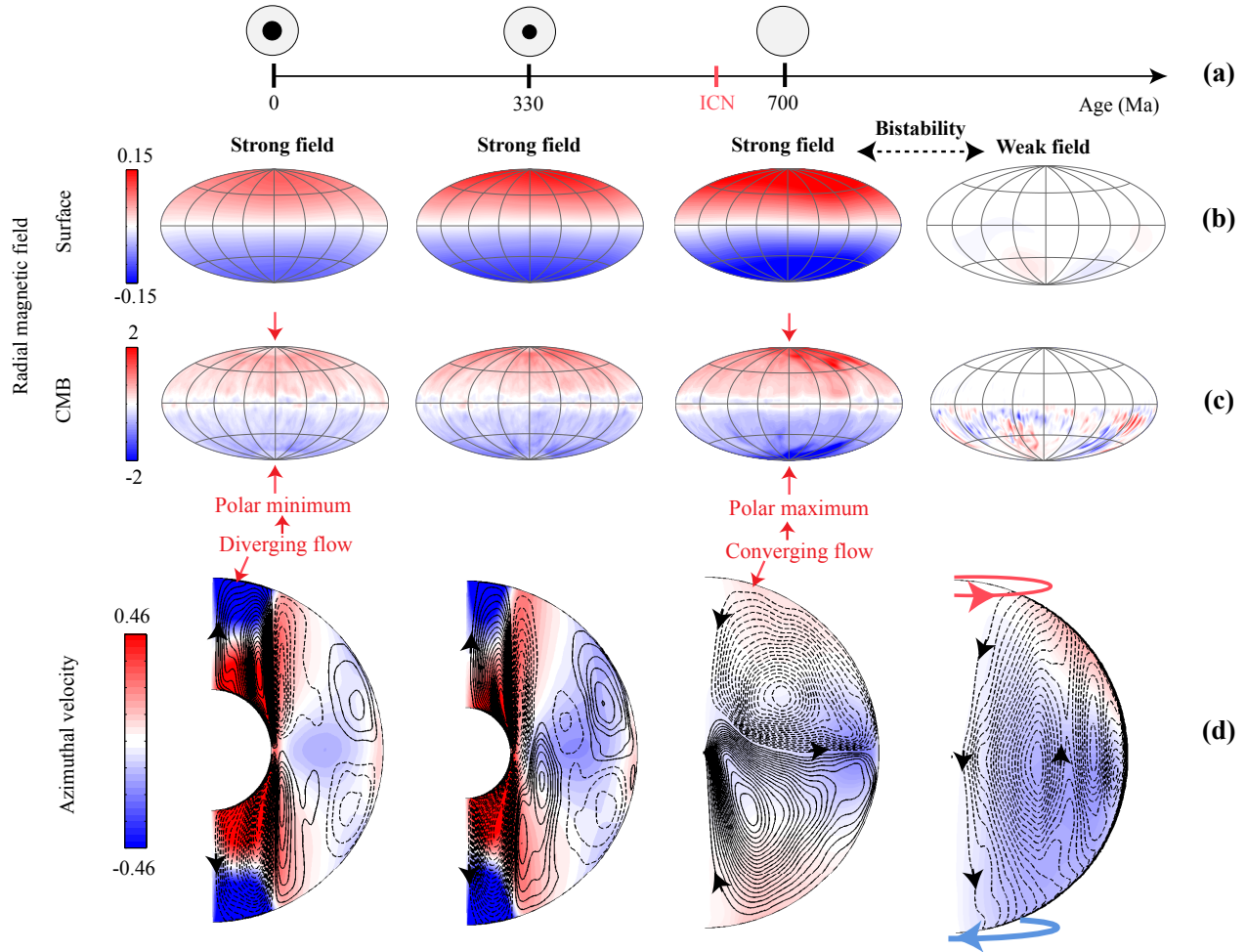


Figure 4: Dynamo structures using constant CMB heat flow History 1 at 0 Ma (first column), 330 Ma (second column) and 700 Ma (third and fourth columns). (a) Age in Ma with corresponding core structure, the black filled circle representing the inner core. (b,c) Radial magnetic field at the surface of the Earth, assuming a 2890 km thick electrically insulating mantle (b) and at the CMB (c), normalized by the present-day rms field intensity at the CMB (Hammer projections, the rotation axis is vertical). Time-averaged magnetic field in the first three columns (strong-field dynamo); snapshots in the fourth column (weak-field dynamo). (d) Meridional cuts of the time-averaged azimuthal velocity, normalized by the present-day rms velocity inside the shell. Contours show streamlines of the meridional circulation which rotates clockwise (solid lines) or anticlockwise (dashed lines).

292 Fig.4 shows our results for the evolution of the magnetic field structure as a function of age at the CMB  
 293 (Fig.4c) and at the Earth's surface (Fig.4b), as obtained in dynamo simulations defined using core History 1.

294 At all ages when an inner core is present, the CMB field is dominated by an axial dipole (first and second  
 295 panels in Fig.4c and  $f_{\text{dip}}$  in Table 1). As a result, the surface field is also dominated by an axial dipole  
 296 (Fig.4b, first and second panels), with a mean axial dipole Gauss coefficient always larger by a factor 20 or  
 297 more than other mean Gauss coefficients. Note that  $f_{\text{dip}}$  increases slightly with age (Table 1), meaning that  
 298 the dipolarity of the field increases back in time. Because the magnetic field is dipole dominated, it is mainly  
 299 symmetric with respect to the equator, showing no particular localization in one hemisphere. Our post-ICN  
 300 dynamo simulations are all characterized by a ratio of magnetic to kinetic energy larger than 1 and an Elsasser  
 301 number larger than 10 (Table 1); they are therefore in the so-called *strong-field regime* (e.g. Roberts, 1988).  
 302 Such a dipole-dominated regime has been extensively studied and results from field generation by drifting  
 303 columnar flows (e.g. Olson et al., 1999; Aubert et al., 2008), mainly symmetric with respect to the equator  
 304 (first two panels in Fig.4d).

305 The above dipolar strong-field state is also stable prior to ICN (Table 1 and third column in Fig.4).  
 306 However, prior to ICN, an additional solution emerges and is shown in the fourth column of Fig.4. This  
 307 second dynamo solution is in a weak-field regime where both the ratio of magnetic to kinetic energy and the  
 308 Elsasser number are smaller than 1 (Table 1). The weak-field dynamo state is characterized by a multipolar  
 309 field (as shown by the value of  $f_{\text{dip}}$  in Table 1), which reverses frequently. We record an average of 49 apparent  
 310 polarity reversals per magnetic diffusion time in the weak-field state, whereas the corresponding strong-field  
 311 dynamo does not reverse in one or two diffusion times. The weak field is also strongly hemispherical with  
 312 a magnetic field 6 times more intense in one hemisphere than in the other at the CMB and 2 times at the  
 313 Earth's surface.

314 This hemispherical magnetic field is associated with a strongly asymmetric time-averaged flow, shown in  
 315 the fourth panel of Fig.4d, which contrasts with the equatorially symmetric flow in the strong-field regime  
 316 (third panel in Fig.4d). To characterize the symmetry of the time-averaged flow we measure the ratio of  
 317 the kinetic energy  $K_a$  of the antisymmetric time-averaged flow to the total kinetic energy  $K$  of the time-  
 318 averaged flow. At 700 Ma with core History 1, the ratio  $K_a/K$  is equal to 0.25 in the weak-field state  
 319 whereas it is equal to 0.06 in the strong-field state. The asymmetric time-averaged flow in the weak-field  
 320 regime is characterized by a large-scale meridional cell that goes through the center of the core and two  
 321 patches of azimuthal velocity forming two large-scale vortices of opposite sign, one in each hemisphere (blue  
 322 and red arrows in the fourth panel of Fig.4d). This type of convection has been named *EAA* (equatorially-  
 323 antisymmetric and axisymmetric) convection and its dynamics has been described in detail in Landeau and  
 324 Aubert (2011). Because it relies on the possibility of axial flow going through the center, this type of  
 325 convection is suppressed by an active inner core, and is therefore not observed after ICN.

326 When bistability occurs prior to ICN, the final state of the dynamo depends on initial conditions: an

327 infinitesimally small initial magnetic field leads to a weak-field dynamo whereas a strong enough initial  
 328 magnetic field leads to a strong-field dynamo. Bistability between the strong-field and weak-field states is  
 329 marginal. We find that the weak-field regime is stable between  $p = 9.31 \times 10^{-8}$  and  $p = 2.77 \times 10^{-7}$  at the  
 330 Ekman number of our pre-ICN simulations (Table 1), a very narrow stability domain considering that the  
 331 convective power varies by about two orders of magnitude between 0 Ma and 1000 Ma in our core evolution  
 332 models. As a result, whether or not the dynamo reaches the weak-field regime is sensitive to the core evolution  
 333 scenario; this is illustrated by our core History 2 which never reaches the stability domain of the weak-field  
 334 regime and remains in the strong-field dipolar regime prior and after ICN (Table 1).

335 Despite this narrow stability domain, we find that, at all pre-ICN ages where it is not stable, the weak-field  
 336 regime is metastable: starting from an infinitesimally small magnetic field, the weak-field state is maintained  
 337 for 0.2 to 1 magnetic diffusion times before finally transitioning to the strong-field dipolar state. We do not  
 338 observe any metastability of the weak-field state after ICN.

#### 339 *4.2. Evolution of magnetic field morphology in the strong-field regime*

340 Our core History 2 predicts that the dynamo might have spent the last 2 Ga exclusively in a strong-field  
 341 dipolar regime. In this section, we investigate the effect of ICN on the magnetic field morphology within the  
 342 strong-field dynamo regime.

##### 343 *4.2.1. Surface field morphology: octupole strengthening with age*

344 Although the strong-field dynamo remains dominated by an axial dipole at all ages (Fig.4bc), secondary  
 345 morphological changes at Earth’s surface can be quantified by computing the first Gauss coefficients of the  
 346 surface field. Fig.5 shows the evolution of the Gauss coefficient ratios  $G_2$  and  $G_3$  of the time-averaged field  
 347 in the strong-field dynamo state. The ratio  $G_2$  of the axial quadrupole Gauss coefficient to the axial dipole  
 348 Gauss coefficient shows no consistent trend with age, fluctuating within the 1% range (Fig.5a). In contrast,  
 349 the axial octupole coefficient ratio  $G_3$  progressively increases with age as the inner core vanishes; this is  
 350 consistently found for both core evolution scenarios, as shown in Fig.5a. Starting from negative present-day  
 351 values,  $G_3$  changes sign within the last 330 Ma and reaches positive values of about 4 – 5% around ICN. For  
 352 ages larger than ICN,  $G_3$  decreases with age for core History 2, whereas it remains approximately constant  
 353 for core History 1.

##### 354 *4.2.2. Dynamical origin of the octupole strengthening*

355 In what follows, we interpret the increase in octupole strength as a result of a purely geometric effect as  
 356 the inner core shrinks.

357 After ICN (first and second panels in Fig.4d), the strong buoyancy flux at the ICB induces strong up-  
358 wellings that rise vertically to the poles below the CMB, feeding two meridional cells that are associated  
359 with anticyclonic polar vortices below the CMB. These polar flows have been documented in previous studies  
360 (Olson and Aurnou, 1999; Sreenivasan and Jones, 2005). As a result of the Taylor-Proudman constraint,  
361 which forces the flow to be two-dimensional in rapidly rotating systems, the width of the polar meridional  
362 cells in the first and second panels of Fig.4d is equal to the width of the *tangent cylinder* (an imaginary  
363 cylinder tangent to the inner core and aligned with the rotation axis).

364 In contrast, prior to ICN, we observe downwellings near the poles below the CMB: convection, now  
365 driven at the CMB by core cooling alone, forms downwellings that detach from the CMB and plunge along  
366 the rotation axis (third panel in Fig.4d). Without an inner core and therefore a tangent cylinder, polar flows  
367 become coupled with the rest of the sphere: the polar downwellings merge with two meridional cells that  
368 span the entire outer core.

369 To understand how the above changes in polar flows affect the magnetic field morphology at the CMB  
370 (three first panels in Fig.4c), it is important to recall that convergent flows below the CMB tend to collect  
371 field lines and amplify the magnetic field by stretching whereas divergent flows tend to advect the field lines  
372 away, producing a local minimum in field intensity, as described in previous studies (e.g. Aubert et al., 2008).  
373 In the presence of an inner core, the flow upwellings induce a divergent flow below the poles (two first panels in  
374 Fig.4d) and, therefore, produce a local minimum in magnetic field intensity there (two first panels in Fig.4c).  
375 As a result, the width of the polar upwellings, dictated by the width of the tangent cylinder, controls the size  
376 of the polar minimum in magnetic intensity at the CMB. This explains why the polar minimum in magnetic  
377 intensity gets narrower with age as the inner core shrinks (Fig.4c, two first panels). In contrast, prior to ICN,  
378 the polar downwellings induce a convergent polar flow below the CMB which amplifies magnetic field there,  
379 and causes a polar maximum in radial field intensity at the CMB (Fig.4c, third panel).

380 Finally, the above transition from polar minimum in magnetic field intensity to polar maximum at the  
381 CMB as the inner core vanishes is directly responsible for the increase in axial octupole component with age  
382 at the Earth's surface. Given the structure of the axial dipole and the axial octupole (Fig.5b), a wide polar  
383 minimum in intensity at the CMB, as found in the present-day model (Fig.4c), requires an axial octupole of  
384 opposite sign compared to the axial dipole. This explains the negative  $G_3$  value found in our present-day  
385 dynamos (Fig.5a). Conversely, obtaining a local polar maximum prior to ICN (700 Ma in Fig.4c), requires  
386 the axial octupole to be of same sign as the axial dipole (Fig.5b), corresponding to a positive  $G_3$  value at  
387 Earth's surface (Fig.5a). This also explains why the increase in octupole is progressive from present-day to  
388 ICN (Fig.5a): as the tangent cylinder shrinks, the width width of the polar intensity minimum decreases,  
389 implying greater contribution from higher harmonics of the field and relatively less contribution from the

390 negative octupole.

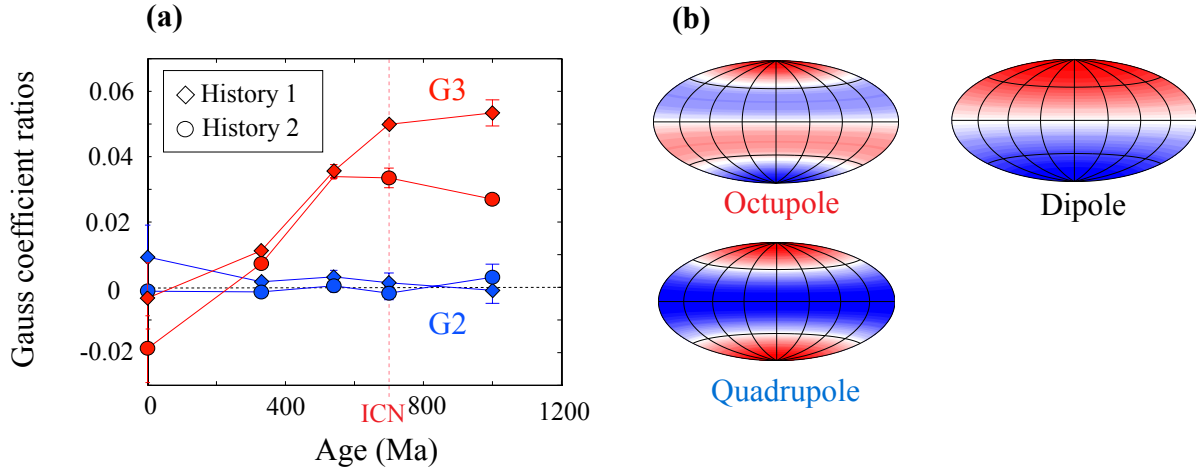


Figure 5: (a) Evolution of mean Gauss coefficient ratios as a function of age obtained in dynamo simulations in the strong-field dynamo regime defined using core History 1 (diamonds) and core History 2 (circles). Red symbols: mean ratio  $G_3$  of the axial octupole coefficient to the axial dipole coefficient. Blue symbols: mean ratio  $G_2$  of the axial quadrupole coefficient to the axial dipole coefficient. Vertical bars denote errors on mean Gauss coefficient ratios. (b) Radial magnetic field structure of the axial dipole, the axial octupole and the axial quadrupole in Hammer projection (the rotation axis is vertical).

## 391 5. Evolution of field intensity with age

### 392 5.1. Weak-field dynamo regime

393 The red squares in Fig.6 show the evolution of the dipole moment in our dynamo simulations, normalized  
 394 to the present-day. The most striking feature is the difference in dipole moment between the strong-field and  
 395 weak-field dynamo states: the dipole moment in the weak-field state is up to 70 times weaker than its value  
 396 in the strong-field state at a given age. Low dipole intensity in the weak-field regime results partly from the  
 397 magnetic field being multipolar, and partly from the magnetic field intensity inside the core being weaker  
 398 than in the strong-field regime (blue squares in Fig.6).

### 399 5.2. Strong-field dynamo regime

#### 400 5.2.1. Internal versus surface field intensity

401 Focusing only on the strong-field dynamo regime in Fig.6, the dipole moment increases monotonically with  
 402 age by a factor 1.6 (core History 1) or 2 (core History 2) until the inner core vanishes. ICN has only a very  
 403 minor effect on surface field intensity, with an increase in dipole moment by a factor 1.2 at most between 540  
 404 Ma and ICN at 700 Ma. For ages larger than 700 Ma, in the absence of an inner core, the dipole moment

405 shows no significant variation given the uncertainties. This increase in dipole intensity with age is unexpected  
 406 and counter-intuitive, in light of the fact that the convective power  $p$  decreases with age, dropping by [more](#)  
 407 [than one order of magnitude](#) between 540 Ma and 700 Ma (Tables 2 and 3, Fig.3).

408 Numerical dynamo investigations (Christensen and Aubert, 2006; Christensen et al., 2009; Aubert et al.,  
 409 2009) find that the rms internal magnetic field strength is controlled by the convective power available to  
 410 balance Ohmic dissipation, provided that the field is dipole-dominated, such that

$$B_{\text{rms}} \propto f_{\text{ohm}}^{1/2} p^{1/3} (\rho\mu)^{1/2} \Omega D, \quad (13)$$

411 where  $f_{\text{ohm}}$  the Ohmic dissipation fraction of the convective power (as introduced in Christensen and Aubert,  
 412 2006). Scaling (13) can be derived from dimensional analysis, assuming that the field strength is independent  
 413 of the rotation rate  $\Omega$  ( $p$  varies as  $\Omega^{-3}$  by definition) (Davidson, 2013), and it successfully explains field  
 414 strength observations for planetary and stellar dynamos (Christensen et al., 2009). Equation (13) can be  
 415 converted into past-to-present day ratios:

$$\frac{B_{\text{rms}}}{B_{\text{rms}0}} \left( \frac{f_{\text{ohm}0}}{f_{\text{ohm}}} \right)^{1/2} = \left( \frac{p}{p_0} \right)^{1/3} \frac{D\Omega}{D_0\Omega_0}. \quad (14)$$

416 The blue curves in Fig.6 show the evolution of the field intensity as predicted by scaling (14), taking  $f_{\text{ohm}} = 1$   
 417 at all times, as usually assumed for Earth's core (Christensen and Aubert, 2006). According to scaling (13),  
 418 magnetic field intensity is positively correlated with the convective power, therefore, the sharp decrease in  
 419 convective power near ICN (between 540 Ma and 700 Ma in Fig.3) is expected to cause a decrease in field  
 420 intensity (blue curves in Fig.6). The increase in dipole moment from present-day to ICN, shown in Fig.6, is  
 421 at variance with this prediction.

422 The above discrepancy between power-based arguments and the evolution of the dipole moment, does  
 423 not, however, originate from an inconsistency with power-based scalings: the internal field intensity in our  
 424 dynamo simulations (blue symbols in Fig.6) does follow scaling (14), with a clear decrease between 540 Ma  
 425 and 700 Ma as the inner core vanishes, trending opposite to the dipole moment. In Supplementary Material,  
 426 we provide further confirmation of the consistency between our simulations and power-based scaling (13).

### 427 5.2.2. Dynamical origin of dipole intensity increase

428 The discrepancy between the evolution of the internal field and the dipole field at the surface can be  
 429 attributed to the depth of the dynamo region, which varies with the buoyancy source distribution  $f_i$  as the  
 430 core evolves. This is illustrated in Fig.7, which compares magnetic energy densities before and after ICN.  
 431 When the inner core is present, the convective power driving dynamo action mainly comes from the buoyancy  
 432 flux at the ICB (i.e.  $f_i \approx 1$ ), through light element and latent heat release. In this case, we obtain deeply-  
 433 seated dynamos where magnetic energy density is high close to the ICB. In contrast, in the absence of an

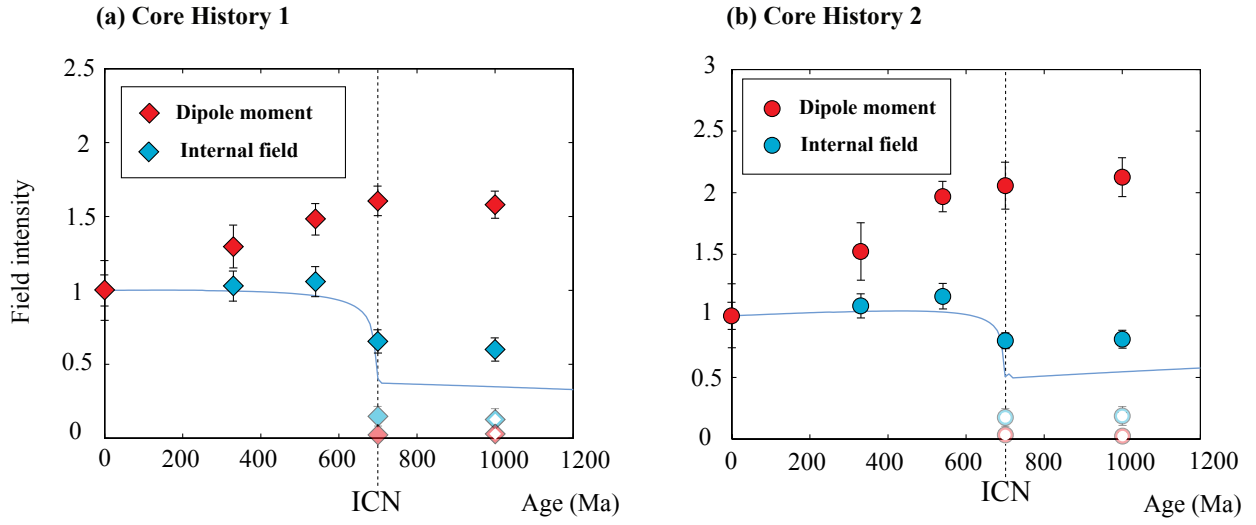


Figure 6: Evolution of magnetic field intensity with age from dynamo simulations using core History 1 (a) and core History 2 (b). Results are shown in terms of past to present-day ratios of dimensional quantities. Red symbols denote dipole moment  $M/M_0$ , blue symbols denote rms magnetic field intensity inside the outer core  $B_{rms}/B_{rms0}$  and blue solid curves show the internal field intensity predicted by the power-based scaling (14). Following Christensen and Aubert (2006), internal and dipole field intensities have been corrected for ohmic dissipation fraction  $f_{ohm}$ . Saturated colors denote strong-field dynamo states and lighter colors weak-field states. Full symbols denote stable solutions; empty symbols denote unstable weak-field solutions that can be maintained for 0.2 to 1.3 magnetic diffusion times before transitioning to a stable strong-field state.

434 inner core, when the destabilizing buoyancy flux comes from the CMB (i.e.  $f_i = 0$ ), the dynamo is shallower,  
 435 with greater magnetic energy density just below the CMB.

436 Because the dynamo region becomes shallower with age, a larger fraction of magnetic energy escapes the  
 437 core, which causes the increase in surface to internal intensity ratio seen in Fig.6. In addition, the magnetic  
 438 field is dominated by larger scales prior to ICN than at present day (Fig.7 and  $f_{\text{dip}}$  in Table 1), which  
 439 contributes slightly to the increase in surface to internal intensity ratio. The shallowing of the dynamo region  
 440 from present-day to ICN, combined with the increase in dipolarity of the field, more than compensate for the  
 441 decrease in power, allowing the dipole moment to increase with age.

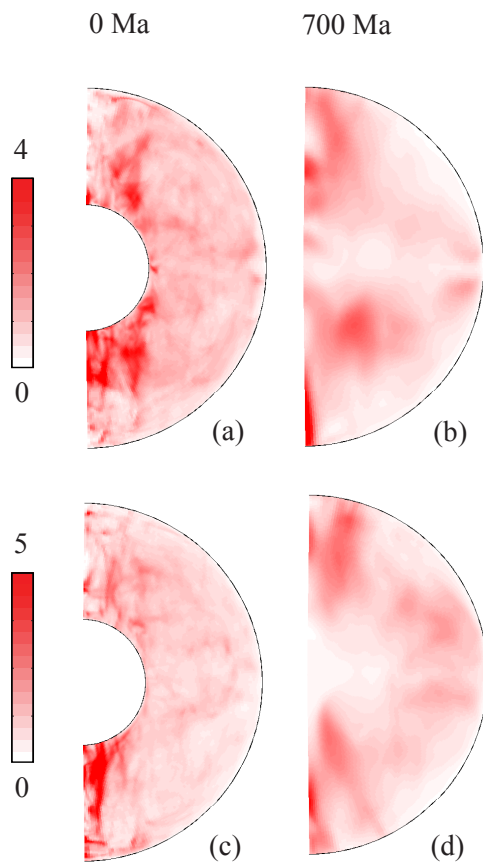


Figure 7: Meridional cuts of the axial magnetic energy density (snapshots normalized by present-day mean energy density) in present-day (0Ma, left) and pre-ICN (700 Ma, right) **strong-field** dynamo simulations defined using History 1 (a,b) and History 2 (c,d).

## 442 6. Discussion and conclusion

443 Our results first indicate that dipole-dominated, strong-field dynamos are stable at any age. Prior to  
444 ICN, though, bistability is observed, indicating that a second regime with a weak, multipolar dynamo field  
445 is possible. Our results largely confirm recent findings of Driscoll (2016), i.e. the possibility of weak-field  
446 dynamos prior to ICN, characterized by an Elsasser number smaller than 1 and a ratio of magnetic to kinetic  
447 energy on the order of 1.

448 In the weak-field dynamo state, the magnetic field is multipolar, with frequent polarity reversals and a  
449 dipole intensity up to 70 times weaker than in the strong-field dynamo state, and which does not conform  
450 to standard dynamo scalings (Christensen and Aubert, 2006; Aubert et al., 2009). A transient weak-field  
451 geodynamo state at or prior to ICN may therefore explain anomalies in the palaeomagnetic record; this  
452 *catastrophic* scenario has been suggested by Driscoll (2016). Because the weak-field dynamo state exists only  
453 prior to ICN, robust anomalies in the palaeomagnetic record could provide an upper bound on the age of the  
454 inner core.

455 No bistability was reported in Driscoll (2016). This leads the author to argue for the above catastrophic  
456 scenario and conclude that the weak-field dynamo state is an obligatory passage close to ICN, with palaeo-  
457 magnetic anomalies as markers of ICN. Because our present results clearly indicate bistability, our conclusions  
458 differ from those of Driscoll (2016): we argue in favor of a simpler, *uniformitarian* scenario in which the geo-  
459 dynamo spent the last 2 Ga, both prior and after ICN, exclusively in a strong-field dipole-dominated regime.  
460 We note that, contrary to our pre-ICN simulations where the inner core has been properly removed, a small  
461 inner core is retained in Driscoll (2016) for numerical reasons. This is however unlikely to explain differences  
462 in stability behavior since retaining a small, passive inner core little affects the solution (Landeau and Aubert,  
463 2011).

464 A major shortcoming of the catastrophic scenario comes from the narrow stability region of the weak-field  
465 dynamo state, which only permits for a threefold variation in convective power, a negligible range relative to  
466 the two orders of magnitude over which power can vary during the past billion years (Figure 3). In addition,  
467 in our bistable dynamos, we did not observe spontaneous transitions from a strong to a weak-field state.  
468 Because palaeomagnetic observations require the geodynamo to be in a strong-field dipolar regime at some  
469 time prior to ICN (Evans, 2006; Biggin et al., 2015; Smirnov et al., 2011), a significant external perturbation  
470 of the dynamo would be needed in order to access the weak-field regime. Variations in the CMB heat flow  
471 could for instance temporarily shut down the dynamo and restart it in the weak-field regime, but this would  
472 require a fine-tuned thermal evolution scenario.

473 In contrast, the uniformitarian scenario is insensitive to the details of the core thermal evolution, as  
474 illustrated by our two core evolution scenarios in the strong-field state. We note for instance that, although

475 we do not explicitly consider the low-conductivity value recently suggested by Konôpková et al. (2016) in  
476 our core evolution models, we do not expect such a scenario to alter our main conclusions. Indeed, lowering  
477 the adiabatic heat flow in History 1, while maintaining the same constant and uniform CMB superadiabatic  
478 heat flow, results in a core evolution identical to History 1, but with a drop in power near ICN smaller by  
479 a factor  $\sim 7$ . Therefore, a low-conductivity scenario would mainly reduce the amplitude of ICN footprints,  
480 without affecting the overall dynamo behavior.

481 The uniformitarian scenario has other strengths. It is consistent with the quasi-stationary reversal state  
482 of the geodynamo inferred from polarity ratios in the palaeomagnetic record during the last two billion years  
483 (Driscoll and Evans, 2016). A dipole-dominated geodynamo during the last 2 billion years is consistent with  
484 palaeomagnetic observations, including inclination frequency distribution (Veikkolainen and Pesonen, 2014),  
485 correlation between paleointensity and inclination (Biggin et al., 2015), latitudinal dependence of paleosecular  
486 variation (Biggin et al., 2008; Smirnov et al., 2011) and paleoclimatic indicators of latitude (Evans, 2006), and  
487 it would furthermore support the Geocentric Axial Dipole hypothesis on which continental drift reconstruction  
488 relies (Evans, 2013). Lastly, the increase in field dipolarity with age suggested by our strong field dynamos  
489 is consistent with paleosecular variations (Smirnov et al., 2011).

490 Long-term trends in paleointensity have long been suspected to bear ICN footprints (e.g. Hale, 1987;  
491 Valet et al., 2014; Biggin et al., 2015) but no uncontroversial trend has been isolated so far (Smirnov et al.,  
492 2016). Our uniformitarian scenario rationalises this lack of trend. The surface magnetic field intensity from  
493 the strong-field dynamo models slowly increases with age from present-day to ICN, with depth changes of  
494 the dynamo region compensating the decrease in internal field predicted by dynamo scaling laws (Stevenson  
495 et al., 1983; Olson, 1981; Aubert et al., 2009). We note that the slow intensity increase of the surface field  
496 predicted by our results applies only to the time that includes ICN, i.e. the last  $\sim 2$  Ga, and cannot be  
497 extended to older times.

498 Rather than paleointensity, our results point towards a long-term evolution in the amplitude of the axial  
499 octupole as a proxy for inner-core growth. We find that, in the strong-field dipole-dominated regime, the  
500 octupole is stronger prior to ICN than at present-day, consistent with previous dynamo simulations (Heimpel  
501 and Evans, 2013). Our results suggest that ICN is marked at the Earth’s surface by a change in slope in the  
502 time-evolution of the Gauss coefficient ratio  $G_3$  associated with the axial octupole: we find that  $G_3$  increases  
503 monotonically from negative values at present day to positive values of the order of 5% at ICN, and then  
504 remains constant (or even decreases) for ages larger than ICN. This increase in octupole strength results from  
505 changes in polar flows caused by a purely geometric effect as the inner core shrinks with age.

506 Analysing anomalies in palaeomagnetic inclinations, Kent and Smethurst (1998) have argued for a rela-  
507 tively strong octupole ( $G_3$  up to  $\approx 25\%$ ) in the Precambrian. A more recent investigation (Veikkolainen and

508 Pesonen, 2014) suggests a smaller value up to 8%, still significantly larger than the value  $1.1\% \pm 1.2\%$  for the  
509 last five million years  $G_3$  (McElhinny, 2004). Our results suggest that the increase in  $G_3$  may be explained  
510 by the shrinking of the inner core, without requiring any heat flux heterogeneities at the CMB (Bloxham,  
511 2000). An important question that needs to be answered by future investigations is whether a change in  
512 slope in  $G_3$  can be resolved in the palaeomagnetic record within the last 1 – 1.5 billion years. In our view,  
513 this would provide a robust palaeomagnetic signature for ICN.

514 Finally, the weak-field dynamo states that pertain to pre-ICN conditions have some unexpected fluid  
515 mechanical properties, including a multipolar and hemispherical magnetic field stable at intermediate rather  
516 than high forcing, at variance with previous studies (Landeau and Aubert, 2011; Christensen and Aubert,  
517 2006). Such peculiarities of the weak-field regime obtained here at low Ekman number call for additional fluid  
518 mechanical analyses applied to planetary dynamos with passive or missing inner core.

519

520 **Acknowledgements:** This work was supported by the National Science Foundation through grant EAR-  
521 1135382 from the Frontiers in Earth System Dynamics program. This work was granted access to the HPC  
522 resources of S-CAPAD, IPGP, France, and to the HPC resources of TGCC, CINES and IDRIS under the  
523 allocation 2016-042122 made by GENCI.

524 **Author contributions:** ML, JA, and PO jointly designed the study, JA and ML conducted the numerical  
525 simulations, ML and PO calculated the thermal evolution models, ML, JA, and PO contributed to the  
526 analysis and interpretation of data; ML, JA and PO wrote the manuscript and approved the submitted  
527 version.

## 528 References

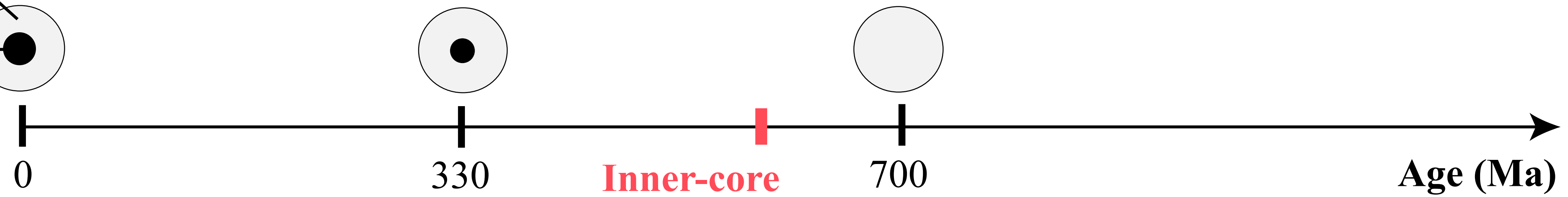
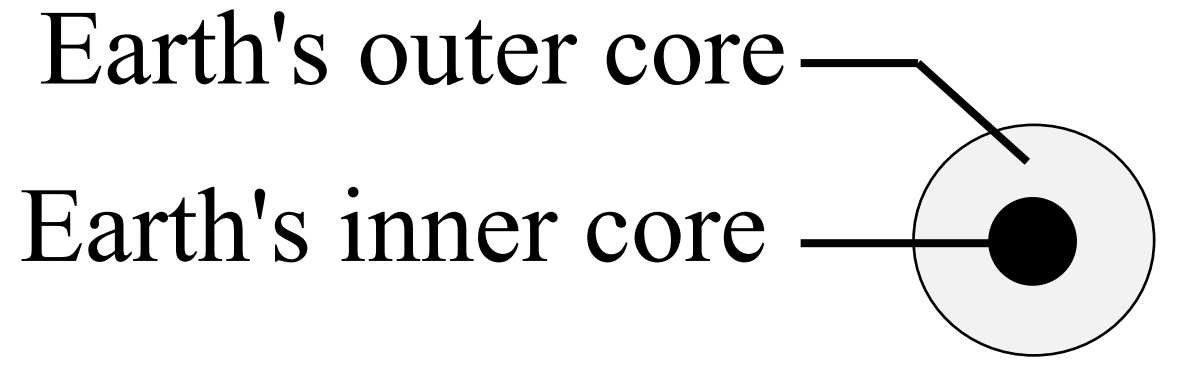
- 529 Aubert, J., Aurnou, J., Wicht, J., 2008. The magnetic structure of convection-driven numerical dynamos.  
530 *Geophys. J. Int.* 172, 945–956.
- 531 Aubert, J., Labrosse, S., Poitou, C., 2009. Modelling the palaeo-evolution of the geodynamo. *Geophys. J.*  
532 *Int.* 179 (3), 1414–1428.
- 533 Badro, J., Siebert, J., Nimmo, F., 2016. An early geodynamo driven by exsolution of mantle components  
534 from earth’s core. *Nature* 536 (7616), 326–328.
- 535 Biggin, A. J., de Wit, M. J., Langereis, C. G., Zegers, T. E., Voute, S., Dekkers, M. J., Drost, K., 2011. Palaeo-  
536 magnetism of Archaean rocks of the Onverwacht Group, Barberton Greenstone Belt (southern Africa):

- 537 Evidence for a stable and potentially reversing geomagnetic field at ca. 3.5 Ga. *Earth Planet. Sci. Lett.*  
538 302 (3-4), 314–328.
- 539 Biggin, A. J., Piispa, E. J., Pesonen, L. J., Holme, R., Paterson, G. A., Veikkolainen, T., Tauxe, L., 2015.  
540 Palaeomagnetic field intensity variations suggest mesoproterozoic inner-core nucleation. *Nature* 526 (7572),  
541 245–248.
- 542 Biggin, A. J., Strik, G. H. M. A., Langereis, C. G., 2008. Evidence for a very-long-term trend in geomagnetic  
543 secular variation. *Nature Geosci.* 1 (6), 395–398.
- 544 Bloxham, J., 2000. Sensitivity of the geomagnetic axial dipole to thermal core–mantle interactions. *Nature*  
545 405 (6782), 63–65.
- 546 Braginsky, S., Roberts, P., 1995. Equations governing convection in Earth’s core and the geodynamo. *Geo-*  
547 *phys. Astrophys. Fluid Dyn.* 79 (1-4), 1–97.
- 548 Christensen, U., Aubert, J., 2006. Scaling properties of convection-driven dynamos in rotating spherical shells  
549 and application to planetary magnetic fields. *Geophys. J. Int.* 166, 97–114.
- 550 Christensen, U. R., Aubert, J., Hulot, G., 2010. Conditions for earth-like geodynamo models. *Earth Planet.*  
551 *Sci. Lett.* 296 (3), 487–496.
- 552 Christensen, U. R., Holzwarth, V., Reiners, A., 2009. Energy flux determines magnetic field strength of  
553 planets and stars. *Nature* 457 (7226), 167–169.
- 554 Davidson, P. A., 2013. Scaling laws for planetary dynamos. *Geophys. J. Int.* 195, 67–74.
- 555 Davies, C., 2015. Cooling history of earth’s core with high thermal conductivity. *Phys. Earth Planet. Int.*  
556 247, 65–79.
- 557 de Koker, N., Steinle-Neumann, G., Vlcek, V., 2012. Electrical resistivity and thermal conductivity of liquid  
558 Fe alloys at high P and T, and heat flux in Earth’s core. *Proc. Nati. Acad. Sci. USA* 109 (11), 4070–4073.
- 559 Denis, C., Rybicki, K., Schreider, A., Tomecka-Suchoń, S., Varga, P., 2011. Length of the day and evolution  
560 of the earth’s core in the geological past. *Astronomische Nachrichten* 332 (1), 24–35.
- 561 Dormy, E., Cardin, P., Jault, D., 1998. MHD flow in a slightly differentially rotating spherical shell, with  
562 conducting inner core, in a dipolar magnetic field. *Earth Plan. Sci. Lett.* 160, 15–30.
- 563 Driscoll, P., 2016. Simulating 2 ga of geodynamo history. *Geophys. Res. Lett.* 43, 5680–5687.

- 564 Driscoll, P., Bercovici, D., 2014. On the thermal and magnetic histories of earth and venus: Influences of  
565 melting, radioactivity, and conductivity. *Physics of the Earth and Planetary Interiors* 236, 36–51.
- 566 Driscoll, P., Evans, D., 2016. Frequency of proterozoic geomagnetic superchrons. *Earth Planet. Sci. Lett.* 437,  
567 9–14.
- 568 Evans, D., 2006. Proterozoic low orbital obliquity and axial-dipolar geomagnetic field from evaporite palae-  
569 olatitudes. *Nature* 444 (7115), 51–55.
- 570 Evans, D., 2013. Reconstructing pre-pangean supercontinents. *Geological Society of America Bulletin* 125 (11-  
571 12), 1735–1751.
- 572 Gomi, H., Ohta, K., Hirose, K., Labrosse, S., Caracas, R., Verstraete, M., Hernlund, J., 2013. The high  
573 conductivity of iron and thermal evolution of the earth’s core. *Phys. Earth Planet. Int.* 224, 88–103.
- 574 Hale, C. J., 1987. Paleomagnetic data suggest link between the Archean-Proterozoic boundary and inner-core  
575 nucleation. *Nature* 329 (6136), 233–237.
- 576 Heimpel, M., Evans, M., 2013. Testing the geomagnetic dipole and reversing dynamo models over earth’s  
577 cooling history. *Phys. Earth Planet. Int.* 224, 124–131.
- 578 Hori, K., Wicht, J., Dietrich, W., 2014. Ancient dynamos of terrestrial planets more sensitive to core-mantle  
579 boundary heat flows. *Planet. Space Sci.* 98, 30–40.
- 580 Kent, D., Smethurst, M., 1998. Shallow bias of paleomagnetic inclinations in the paleozoic and precambrian.  
581 *Earth and Planet. Sci. Lett.* 160 (3), 391–402.
- 582 Konôpková, Z., McWilliams, R. S., Gómez-Pérez, N., Goncharov, A. F., 2016. Direct measurement of thermal  
583 conductivity in solid iron at planetary core conditions. *Nature* 534 (7605), 99–101.
- 584 Labrosse, S., 2003. Thermal and magnetic evolution of the Earth’s core. *Phys. Earth Planet. Int.* 140, 127–143.
- 585 Labrosse, S., 2015. Thermal evolution of the core with a high thermal conductivity. *Phys. Earth Planet. Int.*  
586 247, 36–55.
- 587 Landeau, M., 2013. Two aspects of fluid dynamics in planetary cores. PhD dissertation, Institut de Physique  
588 du Globe de Paris.
- 589 Landeau, M., Aubert, J., 2011. Equatorially asymmetric convection inducing a hemispherical magnetic field  
590 in rotating spheres and implications for the past martian dynamo. *Phys. Earth Planet. Int.* 185 (3-4),  
591 61–73.

- 592 Lay, T., Hernlund, J., Buffett, B. A., JAN 2008. Core-mantle boundary heat flow. *Nature Geosci.* 1 (1),  
593 25–32.
- 594 Le Bars, M., Wiczeorek, M., Karatekin, Ö., Cébron, D., Laneuville, M., 2011. An impact-driven dynamo for  
595 the early moon. *Nature* 479 (7372), 215–218.
- 596 Lister, J. R., 2003. Expressions for the dissipation driven by convection in the Earth’s core. *Phys. Earth*  
597 *Planet. Int.* 140 (1-3), 145–158.
- 598 Macouin, M., Valet, J., Besse, J., 2004. Long-term evolution of the geomagnetic dipole moment. *Phys. Earth*  
599 *Planet. Int.* 147 (2-3), 239–246.
- 600 Marti, P., Schaeffer, N., Hollerbach, R., Cébron, D., Nore, C., Luddens, F., Guermond, J.-L., Aubert, J.,  
601 Takehiro, S., Sasaki, Y., et al., 2014. Full sphere hydrodynamic and dynamo benchmarks. *Geophys. J. Int.*  
602 197 (1), 119–134.
- 603 McElhinny, M., 2004. Geocentric axial dipole hypothesis: a least squares perspective. *Timescales of the*  
604 *paleomagnetic field*, 1–12.
- 605 Ohta, K., Kuwayama, Y., Hirose, K., Shimizu, K., Ohishi, Y., 2016. Experimental determination of the  
606 electrical resistivity of iron at earth’s core conditions. *Nature* 534 (7605), 95–98.
- 607 Olsen, N., Lühr, H., Finlay, C., Sabaka, T., Michaelis, I., Rauberg, J., Tøffner-Clausen, L., 2014. The chaos-4  
608 geomagnetic field model. *Geophys. J. Int.* 197 (2), 815–827.
- 609 Olson, P., 1981. A simple physical model for the terrestrial dynamo. *J. Geophys. Res.* 86 (NB11), 875–882.
- 610 Olson, P., Aurnou, J., 1999. A polar vortex in the Earth’s core. *Nature* 402, 170–173.
- 611 Olson, P., Christensen, U., Glatzmaier, G. A., 1999. Numerical modelling of the geodynamo: mechanisms of  
612 field generation and equilibration. *J. Geophys. Res.* 104 (B5), 10383–10404.
- 613 Olson, P., Christensen, U. R., 2006. Dipole moment scaling for convection-driven planetary dynamos. *Earth*  
614 *Plan. Sci. Let.* 250 (3-4), 561–571.
- 615 Olson, P., Deguen, R., Rudolph, M. L., Zhong, S., 2015. Core evolution driven by mantle global circulation.  
616 *Phys. Earth Planet. Int.* 243, 44–55.
- 617 O’Rourke, J., Stevenson, D., 2016. Powering earth’s dynamo with magnesium precipitation from the core.  
618 *Nature* 529 (7586), 387–389.

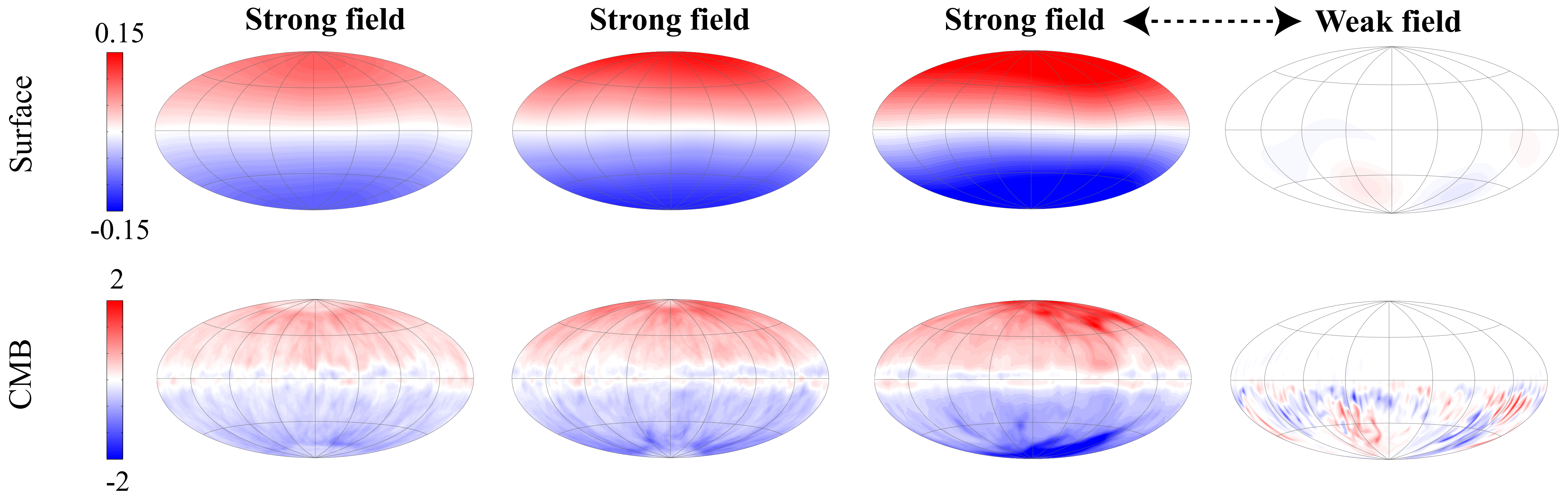
- 619 Pozzo, M., Davies, C., Gubbins, D., Alfè, D., 2013. Transport properties for liquid silicon-oxygen-iron mix-  
620 tures at earth's core conditions. *Phys. Rev. B* 87 (1), 014110.
- 621 Roberts, P., 1988. Future of geodynamo theory. *Geophysical & Astrophysical Fluid Dynamics* 44 (1-4), 3–31.
- 622 Selkin, P., Tauxe, L., 2000. Long-term variations in palaeointensity. *Phil. Trans. R. Soc. Lond. A* 358 (1768),  
623 1065–1088.
- 624 Smirnov, A., Tarduno, J., Evans, D., 2011. Evolving core conditions ca. 2 billion years ago detected by  
625 paleosecular variation. *Phys. Earth Planet. Int.* 187 (3), 225–231.
- 626 Smirnov, A., Tarduno, J. A., Kulakov, E., McEnroe, S., Bono, R., 2016. Paleointensity, core thermal con-  
627 ductivity and the unknown age of the inner core. *Geophys. J. Int.* 205 (2), doi: 10.1093/gji/ggw080.
- 628 Sreenivasan, B., Jones, C. A., 2005. Structure and dynamics of the polar vortex in the earth's core. *Geophys.*  
629 *Res. Lett.* 32 (20), doi: 10.1029/2005GL023841.
- 630 Stevenson, D. J., Spohn, T., Schubert, G., 1983. Magnetism and thermal evolution of the terrestrial planets.  
631 *Icarus* 54 (3), 466–489.
- 632 Tarduno, J., Cottrell, R., Davis, W., Nimmo, F., Bono, R., 2015. A hadean to paleoarchean geodynamo  
633 recorded by single zircon crystals. *Science* 349 (6247), 521–524.
- 634 Tarduno, J. A., Cottrell, R. D., Watkeys, M. K., Hofmann, A., Doubrovine, P. V., Mamajek, E. E., Liu,  
635 D., Sibeck, D. G., Neukirch, L. P., Usui, Y., 2010. Geodynamo, solar wind, and magnetopause 3.4 to 3.45  
636 billion years ago. *Science* 327 (5970), 1238–1240.
- 637 Tauxe, L., 2006. Long-term trends in paleointensity: the contribution of dsdp/odp submarine basaltic glass  
638 collections. *Phys. Earth Planet. Int.* 156 (3), 223–241.
- 639 Valet, J. P., Besse, J., Kumar, A., Vadhakke-Chanat, S., E., P., 2014. The intensity of the geomagnetic field  
640 from 2.4 ga old indian dykes. *Geophys. Geochem. Geosystems*. 15, 2426–2437.
- 641 Veikkolainen, T., Pesonen, L., 2014. Palaeosecular variation, field reversals and the stability of the geodynamo  
642 in the precambrian. *Geophys. J. Int.* 199 (3), 1515–1526.
- 643 Wang, H., Kent, D. V., Rochette, P., 2015. Weaker axially dipolar time-averaged paleomagnetic field based on  
644 multidomain-corrected paleointensities from galapagos lavas. *Proc. Nat. Acad. Sci.* 112 (49), 15036–15041.
- 645 Williams, G., 2000. Geological constraints on the precambrian history of earth's rotation and the moon's  
646 orbit. *Rev. Geophys.* 38 (1), 37–59.



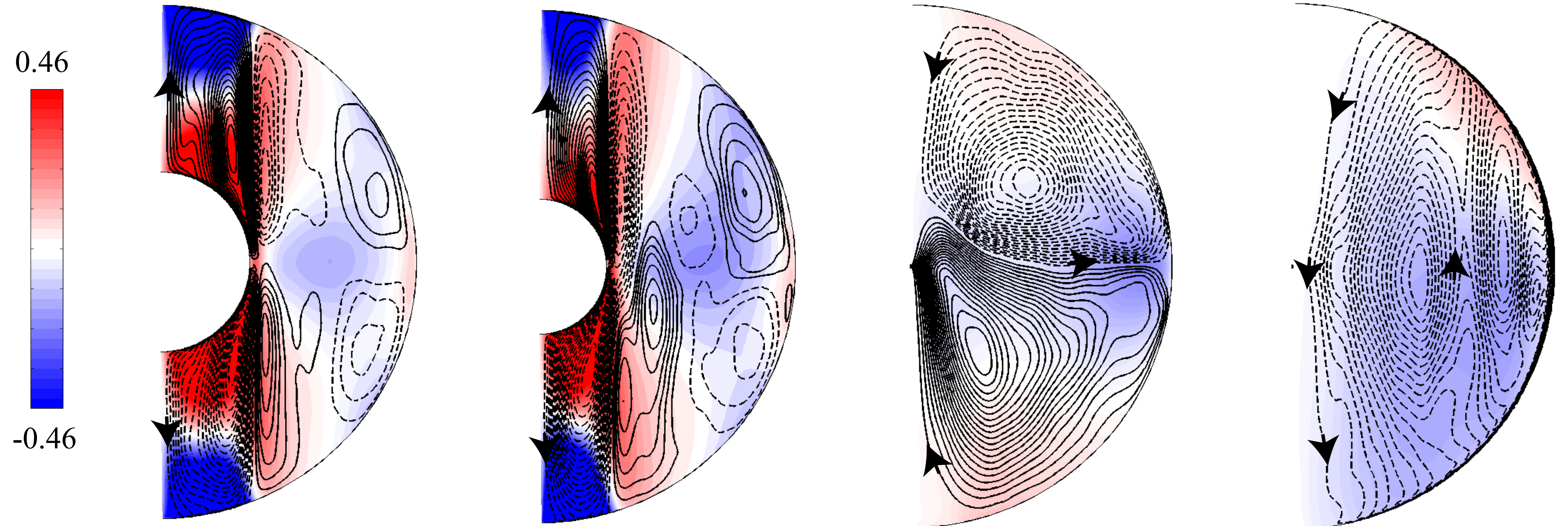
**Inner-core nucleation**

**Bistability**

Radial magnetic field  
(normalized to present-day rms)

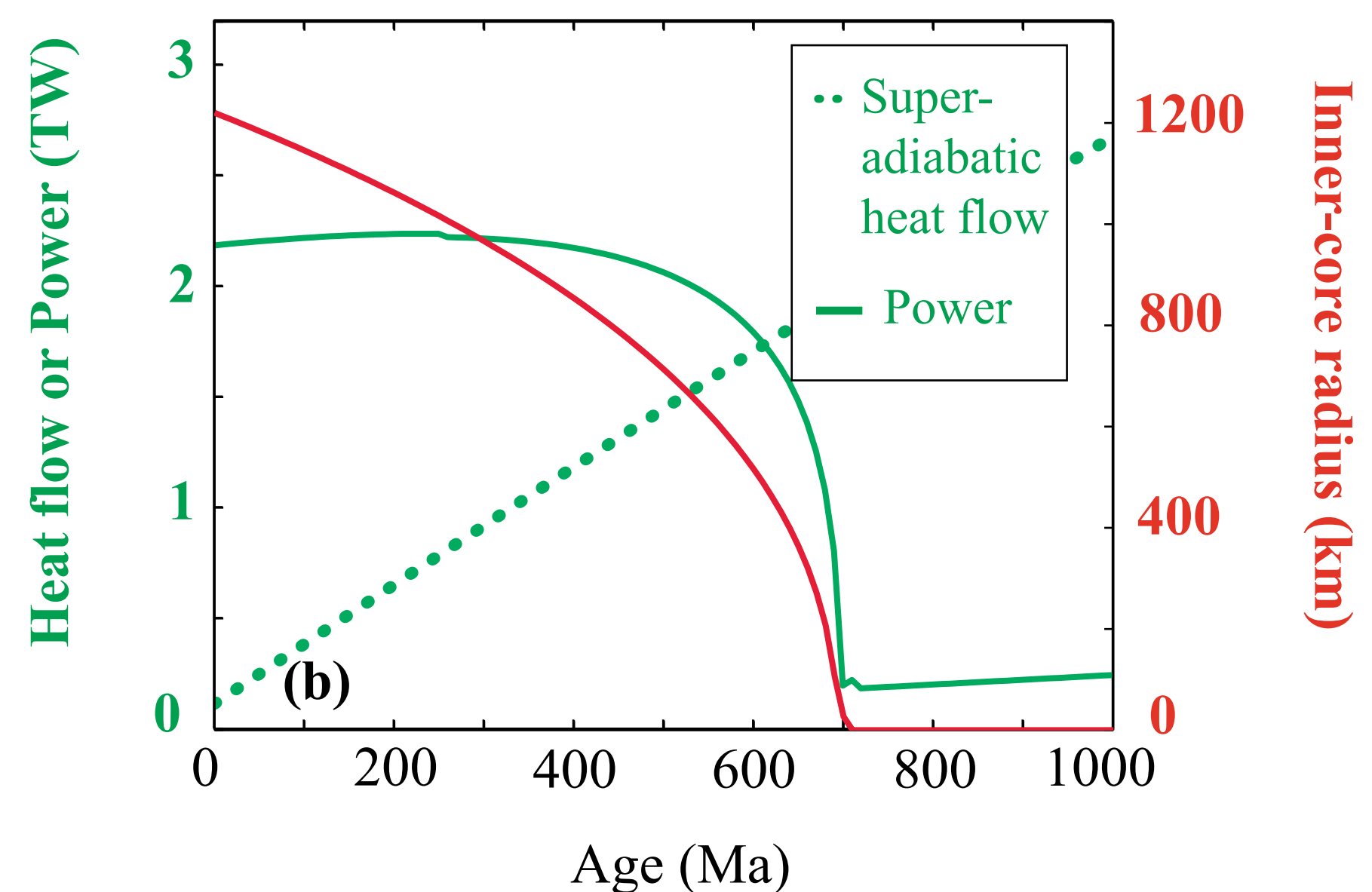
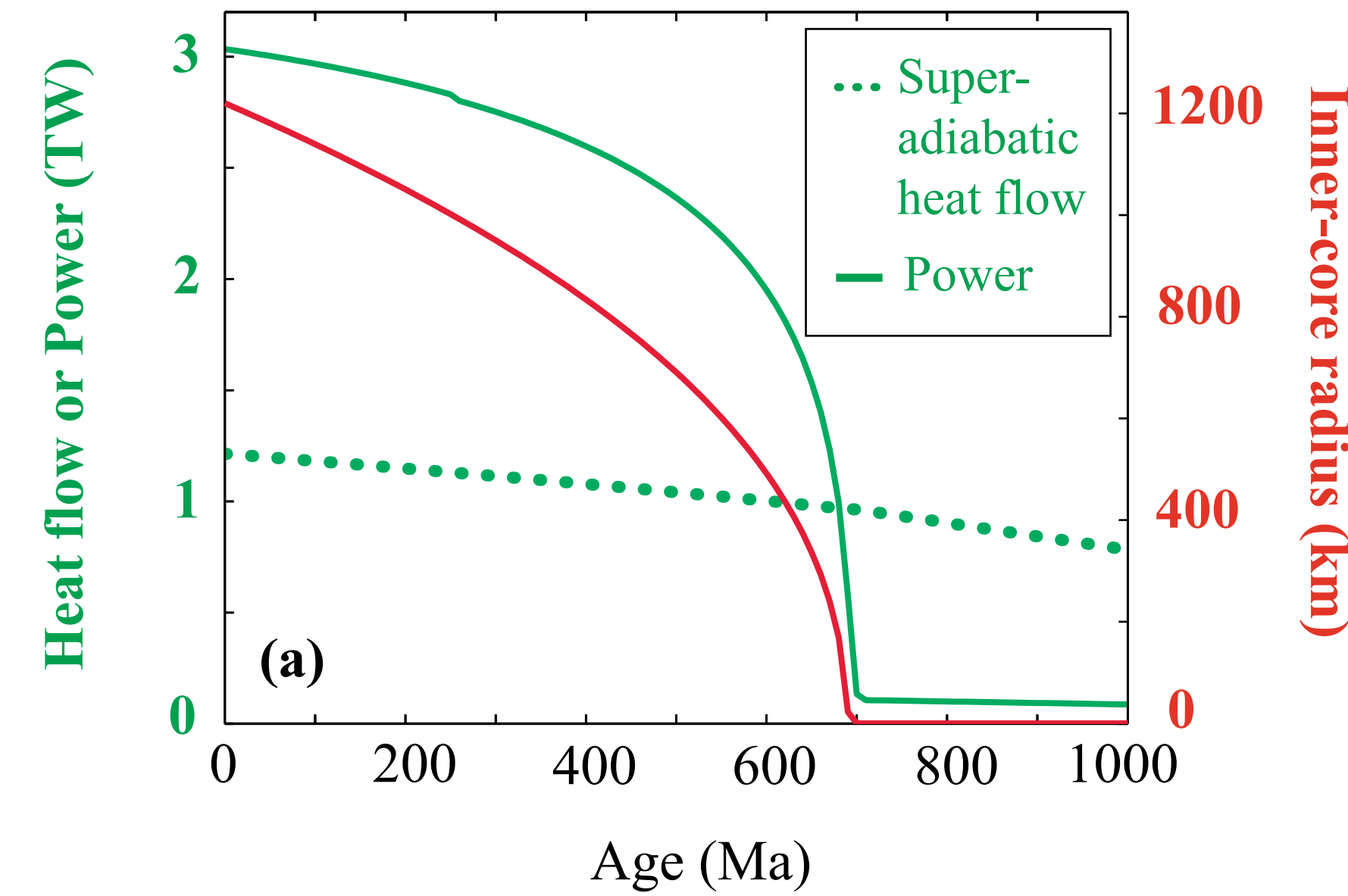


Azimuthal velocity  
& Meridional circulation



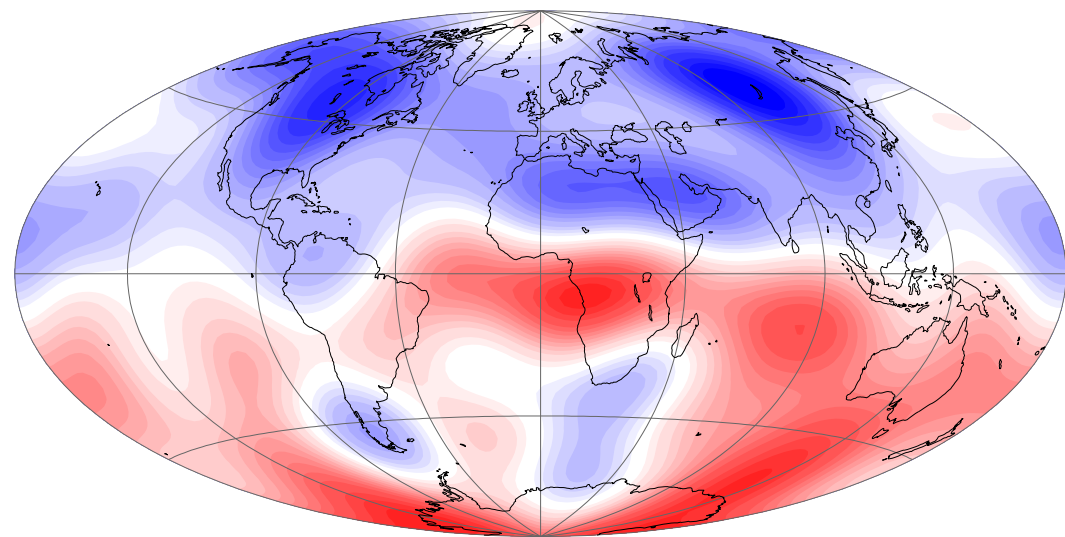
# Core History 1

# Core History 2

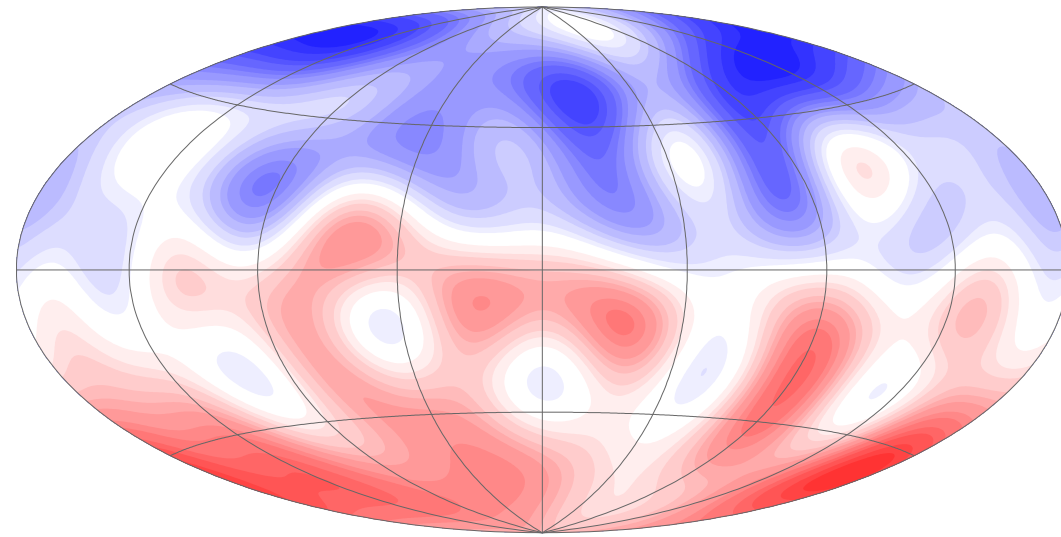


3

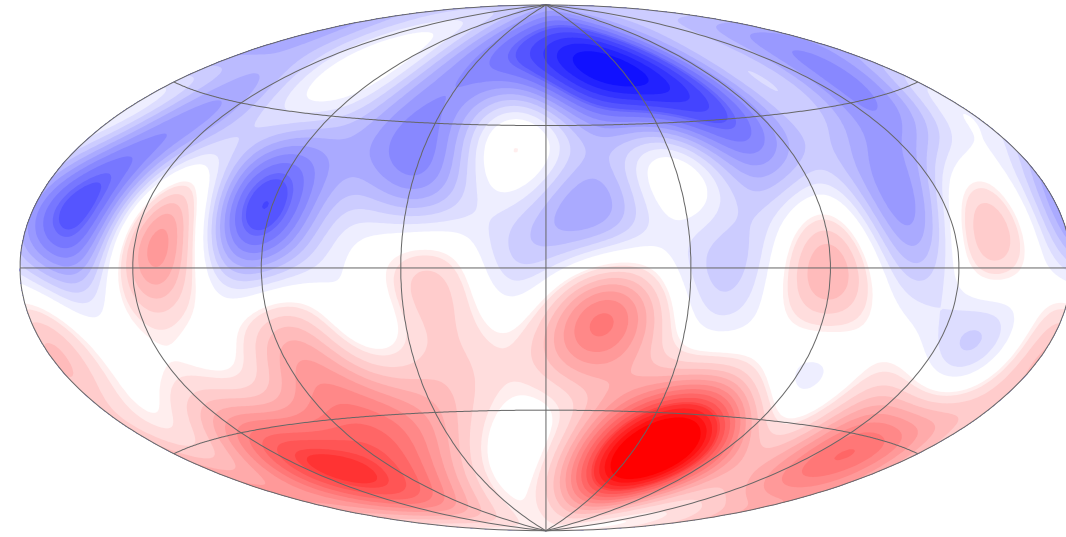
(a) CHAOS-4



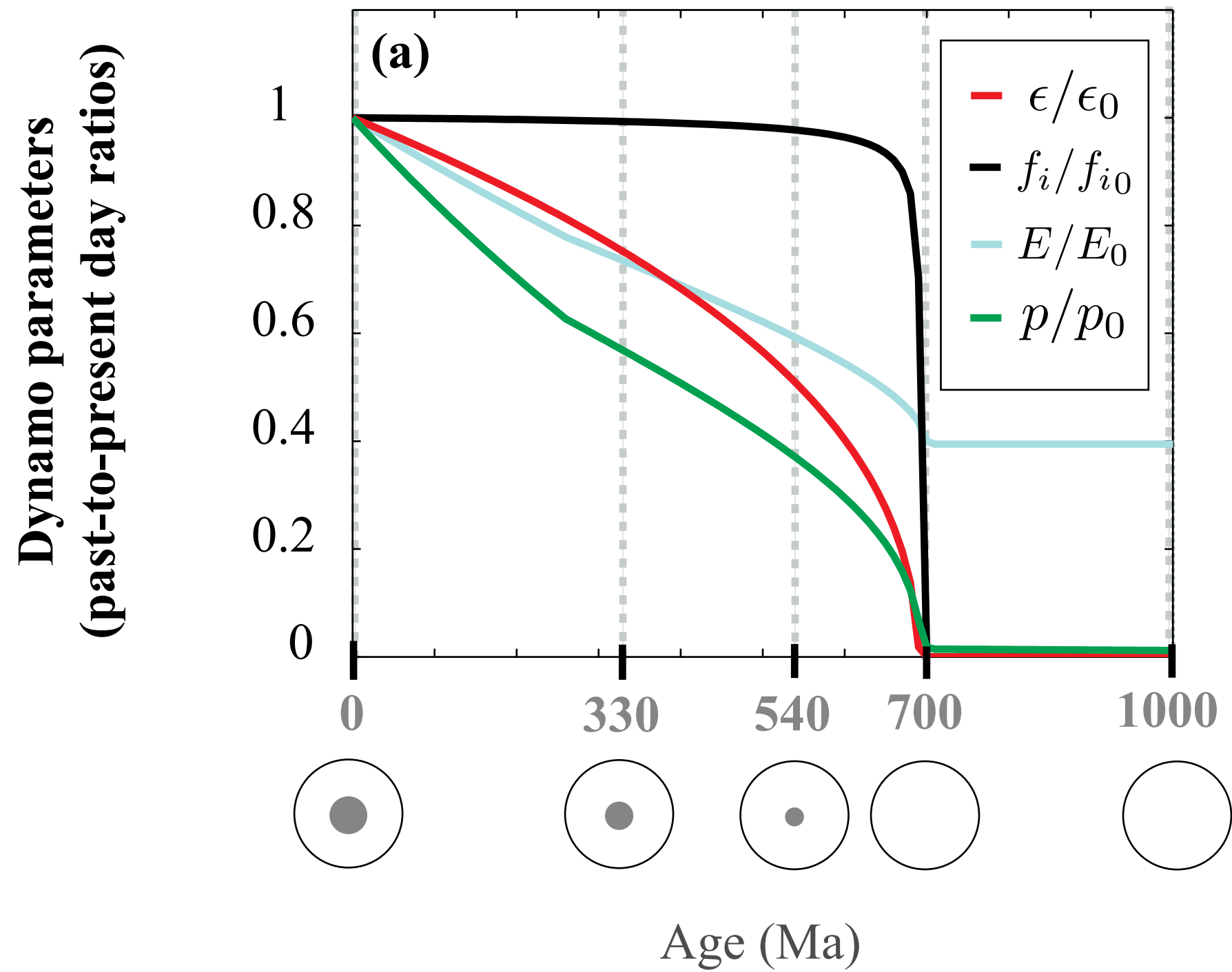
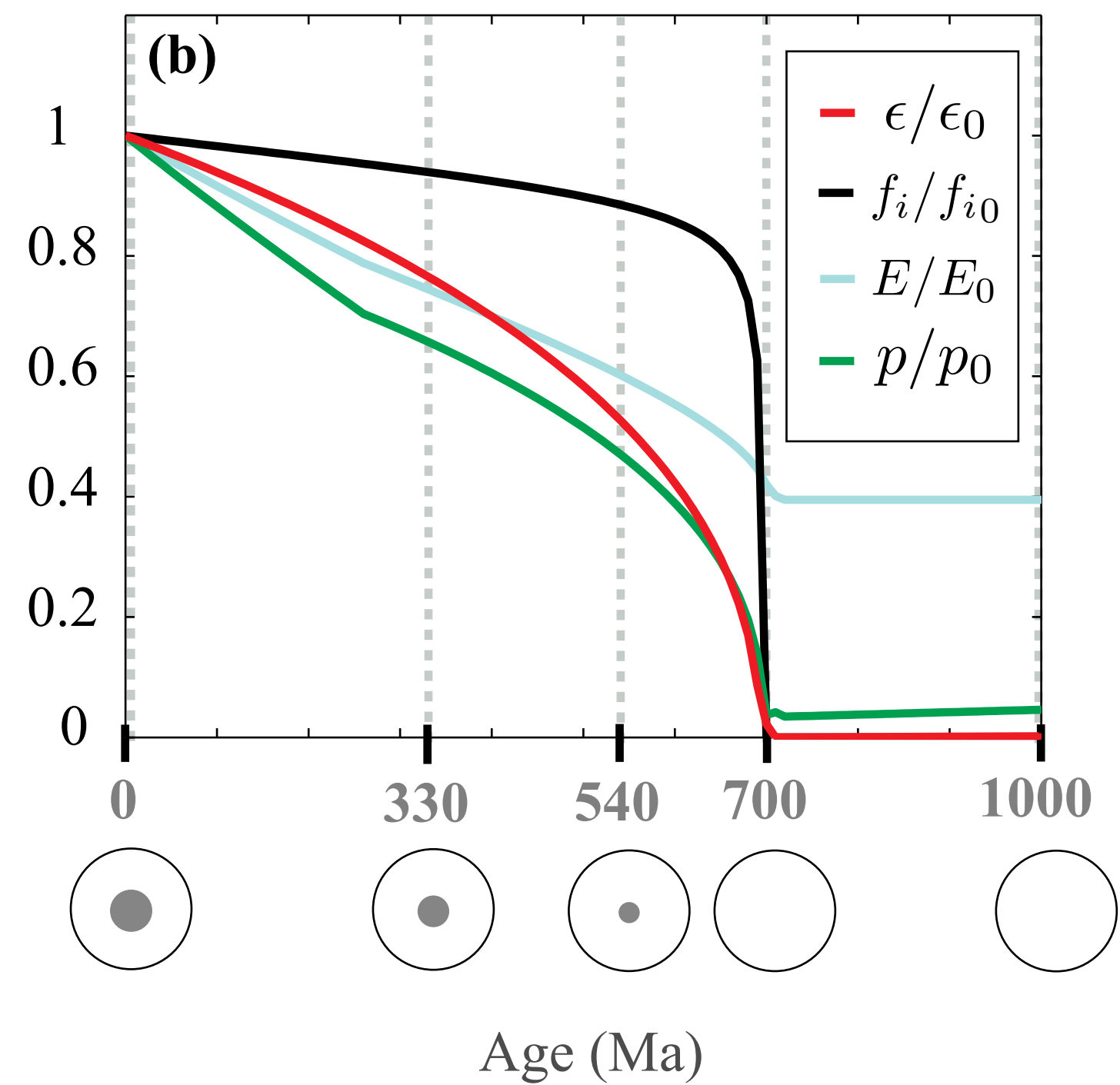
(b)



(c)



-3

**Core History 1****Core History 2**

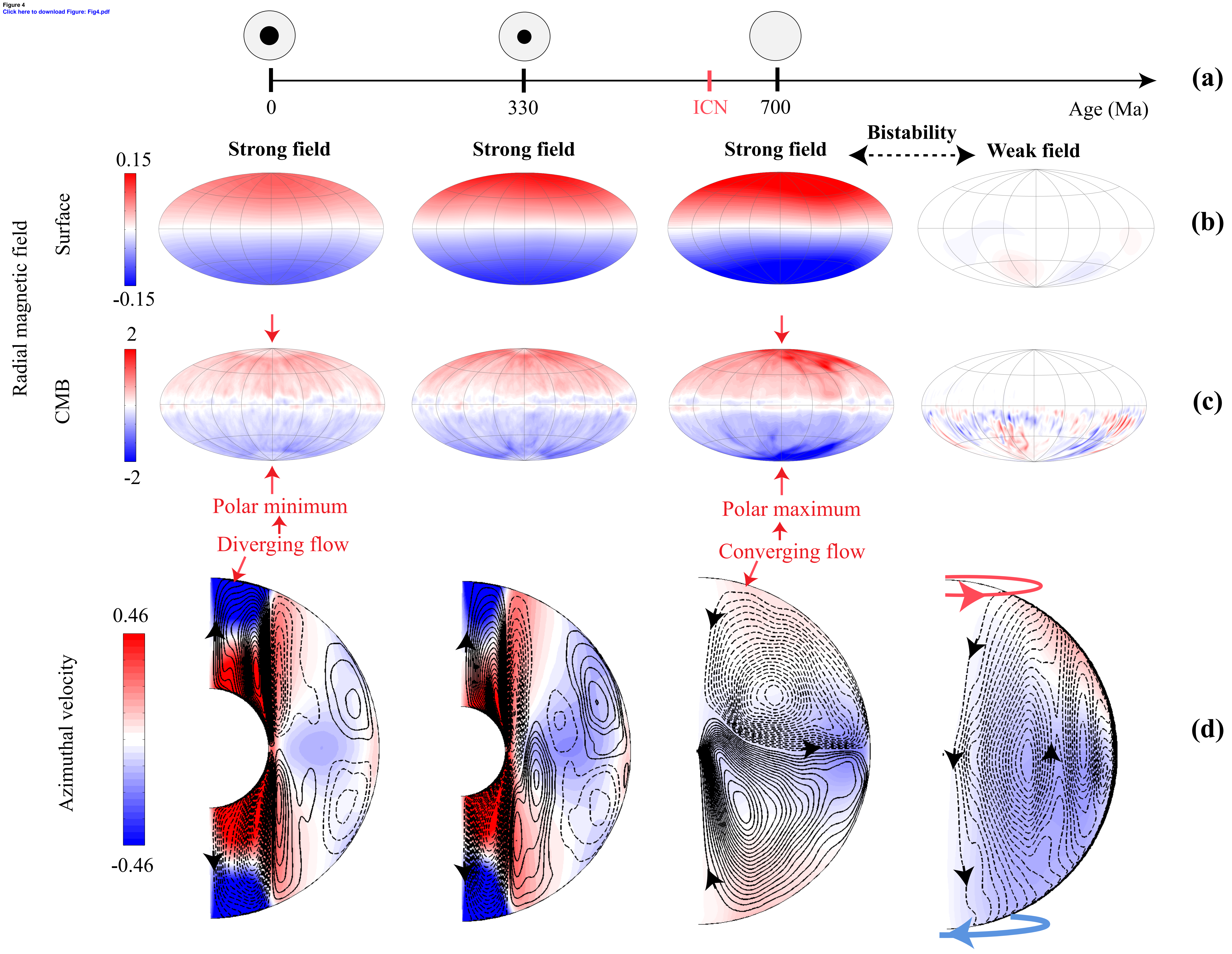
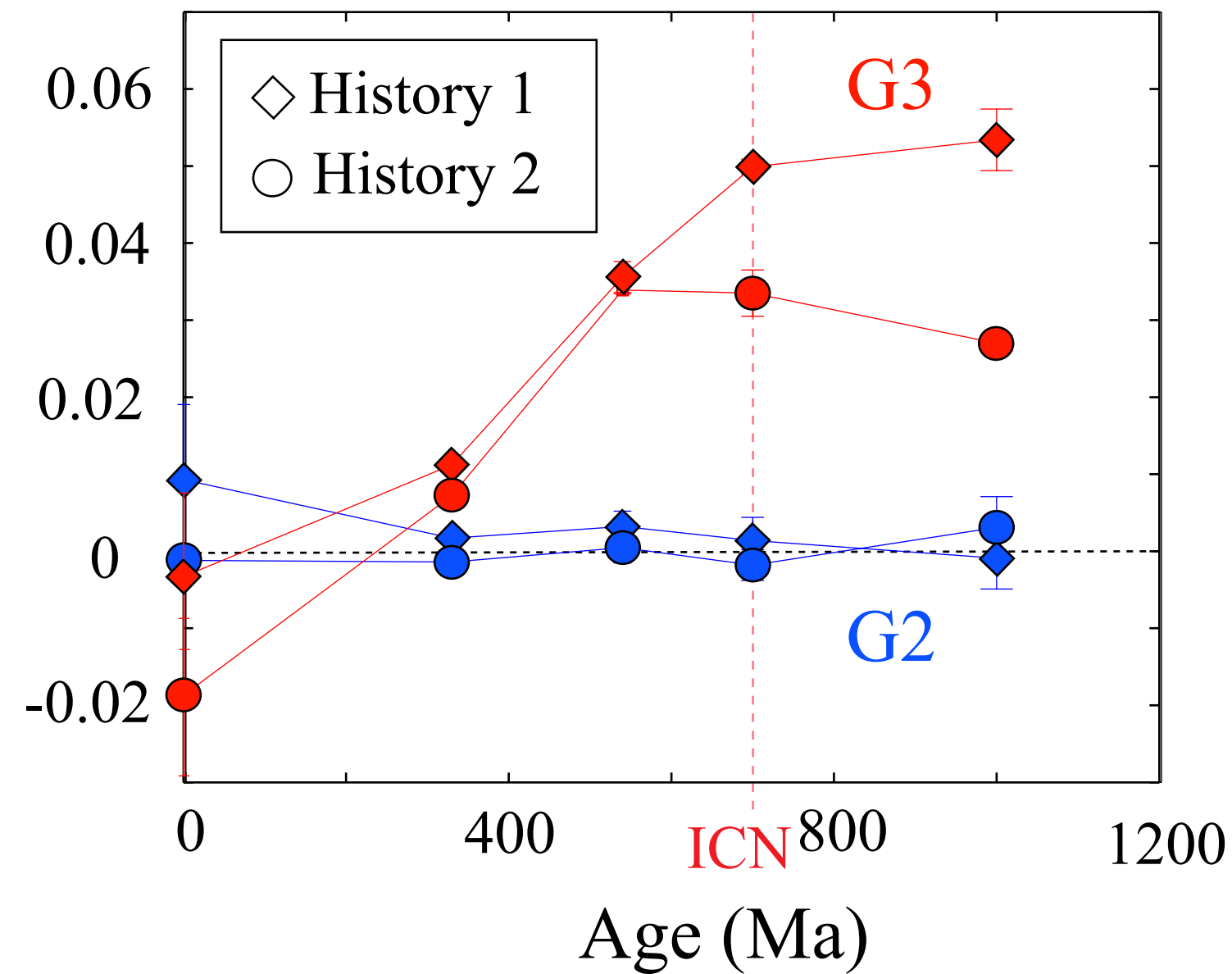
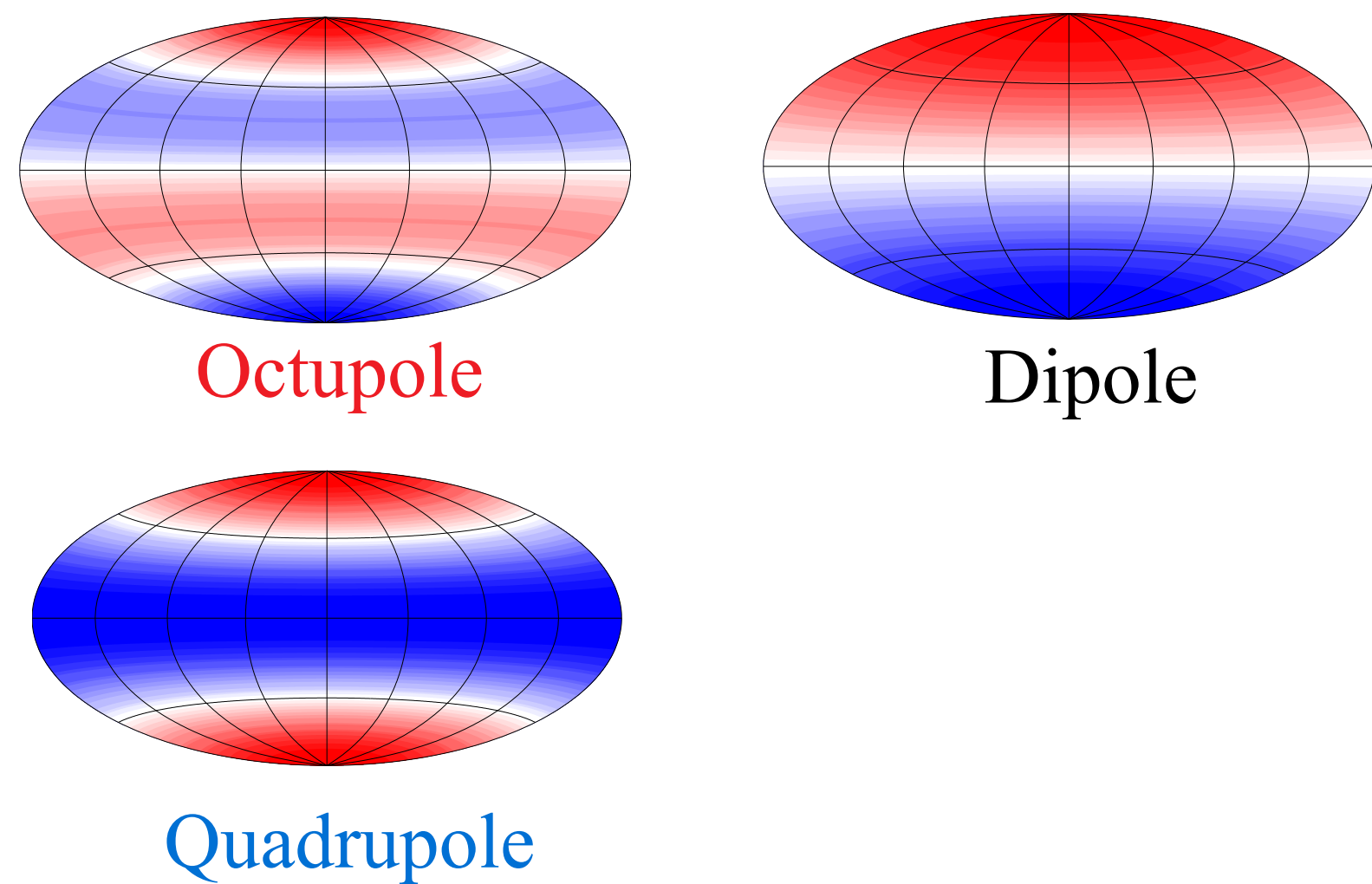


Figure 5  
[Click here to download Figure: Fig5.pdf](#)

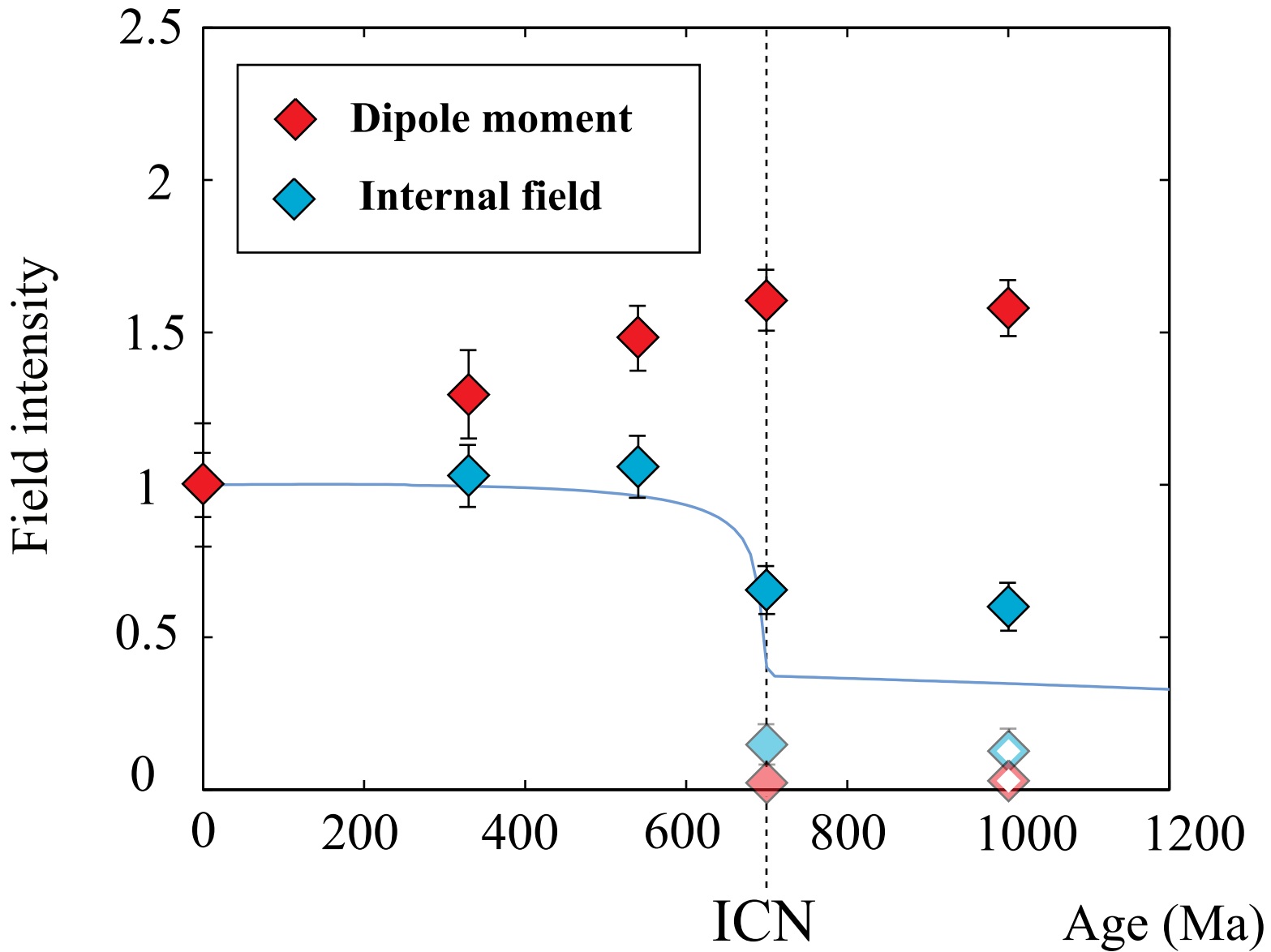
Gauss coefficient ratios



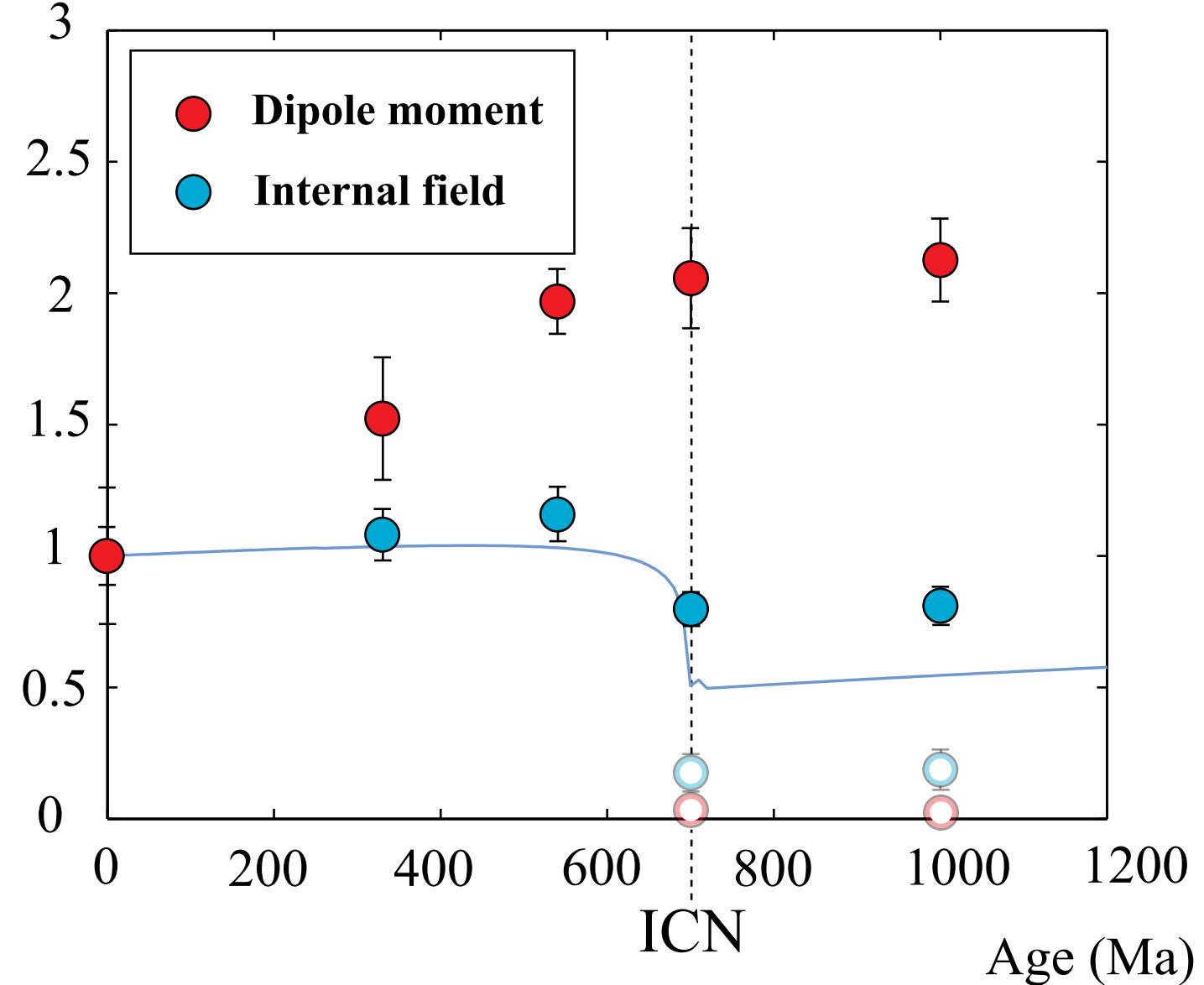
(b)



**(a) Core History 1**



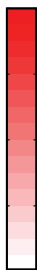
**(b) Core History 2**



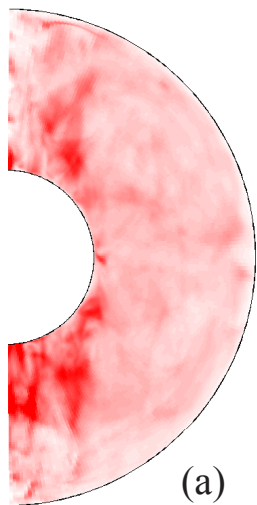
0 Ma

700 Ma

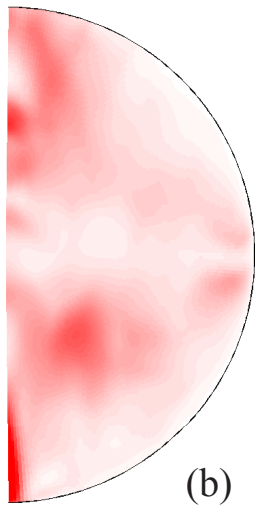
4



0

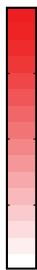


(a)

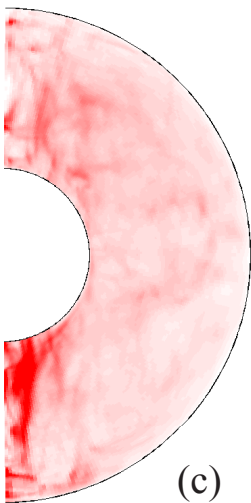


(b)

5



0



(c)



(d)